Materials Advances

ROYAL SOCIETY OF CHEMISTRY

PAPER

View Article Online
View Journal

Cite this: DOI: 10.1039/d5ma01346a

Nitrogen-rich dicyandiamide-grafted graphene oxide catalyst for the synthesis of 1,2,5,6-tetrahydropyridine-3-carboxylates

Tuan Minh Dang,[ab] The-Anh Trinh Duong,[ab] Trung-Nhan Dong Tran[ab] and Hai Truong Nguyen *[ab]

Received 19th November 2025,
Accepted 13th April 2026

DOI: 10.1039/d5ma01346a

rsc.li/materials-advances

In this study, a novel biomass-derived multifunctional catalyst, GO@APTES@DCDA@Sb^{3+}, was successfully synthesized through sequential surface modification and thoroughly characterized by FT-IR spectroscopy, Raman spectroscopy, XRD analysis, ICP-MS analysis, scanning electron microscopy (SEM), energy-dispersive X-ray spectroscopy (EDX) and X-ray photoelectron spectroscopy (XPS). The structural and morphological investigations confirmed the incorporation of nitrogen-rich groups and the uniform coordination of Sb^{3+} ions on the graphene oxide framework, which introduced multiple Lewis acidic sites. Catalytic performance was evaluated in the one-pot solvent-free synthesis of 1,2,5,6-tetrahydropyridine-3-carboxylate derivatives, where GO@APTES@DCDA@Sb^{3+} outperformed other metal-modified catalysts, affording up to 56% yield under optimized conditions (50 °C, 380 min, 5 mg catalyst). The *anti*-isomer was obtained with diastereomeric ratios (dr) up to 90 : 10–100 : 0. Kinetic assessments were conducted to confirm the catalyst's effectiveness in the newly developed reaction. Derived thermodynamic parameters showed $\Delta H^{\ddagger}$ = 0.9571 kJ mol^{-1} and $\Delta S^{\ddagger}$ = −0.0144 kJ mol^{-1} K^{-1}; notably, $\Delta G^{\ddagger}$ was found to increase progressively as a function of temperature. The catalyst showed excellent recyclability, maintaining high activity over repeated cycles, and demonstrated stability with negligible metal leaching. Furthermore, the methodology was successfully extended to gram-scale synthesis, highlighting its practical applicability.

1. Introduction

In recent decades, the intensifying concerns over environmental degradation, resource depletion, and climate change have prompted the scientific community to pursue sustainable alternatives to fossil-based energy and chemical feedstocks.[1] Among the various renewable resources under investigation, biomass which encompasses lignocellulosic residues, agricultural by-products, and other organic wastes has emerged as a particularly attractive candidate due to its abundance, renewability, and carbon-neutral potential.[2] Biomass valorization follows the principles of green chemistry and can help reduce carbon emissions and pollution.[3] A critical area of research in this domain involves the conversion of biomass into functional carbon materials, which are increasingly sought after in energy storage, catalysis, adsorption, and environmental remediation applications.[4] The synthesis of such materials typically involves carbonization processes, wherein the organic constituents of biomass are thermally decomposed under oxygen-deficient or hydrothermal conditions to yield carbon-rich solids.[5] Despite these advances, several challenges remain in the rational design and scalable production of biomass-derived carbon materials.[6] These include the heterogeneous nature of biomass feedstocks, the complexity of reaction pathways during thermal conversion, and the need for precise control over material structure and functionality. Recent studies integrate catalytic or templating strategies during carbonization to improve material performance. Current studies aim to develop efficient and low-cost biomass conversion methods, focusing on structure–property control and process optimization.[7]

Graphene oxide (GO), a highly oxidized derivative of graphene, has attracted substantial attention in materials science and catalysis due to its unique physicochemical properties.[8] Structurally, GO consists of a single-layered sheet of sp^2-hybridized carbon atoms arranged in a hexagonal lattice, extensively functionalized with oxygen-containing groups such as hydroxyl, epoxide, carbonyl, and carboxyl moieties.[9] These functionalities impart hydrophilicity, chemical reactivity, and the potential for further functionalization, making GO an ideal platform for the development of heterogeneous catalysts, sensors, drug delivery systems, and nanocomposites.[9,10] GO is commonly synthesized *via* the oxidation of graphite, with the

[a] Department of Organic Chemistry, Faculty of Chemistry, University of Science, Ho Chi Minh City 700000, Vietnam. E-mail: ngthai@hcmus.edu.vn
[b] Vietnam National University, Ho Chi Minh City 700000, Vietnam

Hummers' method and its modified variants being the most widely employed techniques.[11] In these methods, graphite is treated with strong oxidants such as potassium permanganate in concentrated sulfuric acid, leading to the exfoliation of graphite into oxidized monolayers.[11,12] Post-synthesis, GO can be dispersed in water or polar solvents due to its amphiphilic character, facilitating solution-based processing and composite fabrication. In terms of application, GO has been widely explored across fields such as environmental remediation, electrochemical energy storage, biosensing, and catalysis. Particularly in catalysis, the presence of surface oxygen functionalities allows GO to act as a solid acid catalyst or as a support for active catalytic species, offering high surface area, stability, and recyclability. However, the intrinsic catalytic activity of pristine GO is often limited, necessitating chemical modification to introduce active sites or enhance functionality. GO has attracted considerable interest as a versatile material in organic synthesis owing to its distinctive structural and chemical characteristics.[13] The extensive surface area, along with several oxygen-containing functional groups, such as hydroxyl, epoxy, carbonyl, and carboxyl moieties endows GO with inherent Brønsted acidity and chemical adaptability.[14] These capabilities allow GO to behave as either a direct catalyst or a support for catalytic species, promoting a wide range of organic reactions. As a solid acid catalyst, virgin or functionalized graphene oxide can efficiently facilitate reactions such as esterification, dehydration, and other multicomponent reactions (*e.g.*, Biginelli and Hantzsch condensations) under mild and environmentally friendly conditions.[15,16] Furthermore, its ability to coordinate with transition metals and metal ions (*e.g.*, Fe^{3+}, Cu^{2+}, Ru^{3+}, Sb^{3+}) has resulted in the creation of GO-based Lewis acid catalysts, which are extensively utilized in C–C coupling reactions, oxidation processes,[17] and cyclizations.[18] In photoredox and electrocatalytic applications, GO functions as a redox-active framework that facilitates electron transfer and promotes transformations produced by visible light or electrochemical processes. GO can also be modified with ionic liquids or nitrogen ligands to form hybrid catalysts with higher activity and reusability.[19–21] These compounds have been effectively utilized in eco-friendly synthetic procedures, encompassing solvent-free reactions, microwave-assisted techniques, and reactions performed at ambient temperature.

Heterocyclic compounds, in which at least one heteroatom such as N, O, S, and/or P is incorporated into their carbon rings,[22] have gained great interest from researchers because of their wide range of applications in the materials and pharmaceutical fields.[23–26] Among these heterocyclic compounds, pyridine rings are among the most prevalent cores present in FDA-approved drugs.[27] The substitution of hydrogen atoms on the carbon ring or the nitrogen itself yields several derivatives exhibiting biological activity. Tetrahydropyridine, a partly saturated derivative of pyridine, is a moiety frequently encountered in both synthetic and natural molecules. Derivatives containing tetrahydropyridine have been documented to have a variety of biological activities, including anticancer,[28,29] antitubercular,[29,30] and antioxidant properties[29] in addition to serving as antibiotic adjuvants (Scheme 1).[31]

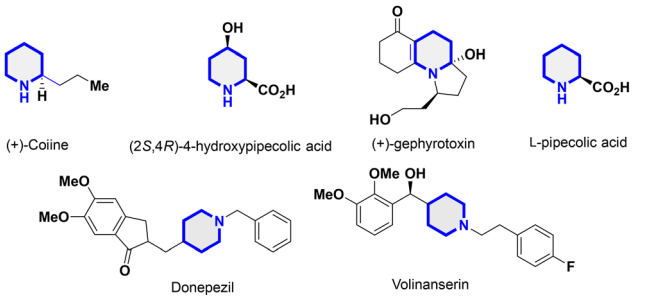

Scheme 1 Biologically active compounds bearing a piperidine skeleton and tetrahydropyridines.

Numerous approaches have been reported for the synthesis of 1,2,5,6-tetrahydropyridines, with common strategies involving the partial reduction of pyridinium salts or 4-piperidones.[32] However, the preparation of substituted tetrahydropyridines, particularly those bearing *N*-aryl functionalities, remains synthetically challenging due to steric and electronic factors. In recent years, several innovative methods have been developed to overcome these difficulties. These include reactions proceeding through iminium ion intermediates,[33] aza-Prins cyclization reaction,[34] phosphine-catalyzed [4+2] π-electron electrocyclic annulations,[35] ionic liquid-supported organocatalyst cyclizations,[36] Wittig rearrangements,[37] aza-Diels–Alder reactions,[38] and cross-metathesis as well as intermolecular allyl silane–nitrone cycloadditions.[39] Despite these advancements, many of the existing protocols still suffer from significant drawbacks, such as harsh reaction conditions, prolonged reaction times, limited substrate scope, low product yields, and reliance on expensive, hazardous, or non-recyclable reagents. Consequently, there is a pressing need to develop more efficient and environmentally benign synthetic routes. In this context, the design of greener catalytic systems, particularly those based on recyclable and non-toxic materials, aligns with the principles of sustainable chemistry and has become a focal point in modern synthetic methodology.

In this work, we reported a promising strategy involves the surface functionalization of GO with organosilanes and nitrogen-rich ligands, followed by the anchoring of metal ions. The APTES (3-aminopropyltriethoxysilane) serves as a silane coupling agent that can graft amino groups onto GO through covalent bonding with hydroxyl groups on the GO surface. Subsequently, DCDA (dicyandiamide), a nitrogen-rich molecule, can be introduced to increase the density of Lewis basic sites. The resulting GO@APTES@DCDA hybrid provides a favorable scaffold for complexation with trivalent antimony ions (Sb^{3+}), forming a multifunctional catalyst system (GO@APTES@DCDA@Sb^{3+}). Comprehensive characterization of the catalyst was carried out through FT-IR, EDX, EDX-mapping, XRD, Raman, SEM, and XPS. In a notable advancement, the GO@APTES@DCDA@Sb^{3+} catalyst was introduced for the first time for the facile synthesis of highly functionalized piperidines *via* a one-pot five-component strategy, delivering the target compounds in good to excellent yields.

2. Results and discussion

2.1. Characterization of catalysts

Scheme 2 illustrates the synthesis pathway involves the surface functionalization of GO with organosilanes and nitrogen-rich ligands, followed by the anchoring of metal ions. Starting from *Manihot esculenta* leaf stalks, carbonization is carried out under a nitrogen atmosphere at 600 °C for 3 h to produce a carbonaceous material.[40] This as-pyrolized material undergoes oxidation *via* the Hummers' method using $KMnO_4$ and $NaNO_3$ in concentrated H_2SO_4, resulting in the formation of GO material.[41] GO is subsequently functionalized with (3-aminopropyl)triethoxysilane (APTES) under reflux in toluene at 100 °C for 12 h, yielding GO@APTES.[42] The obtained material is further treated with dicyandiamide (DCDA) and triethylamine (Et_3N) in ethanol at 65 °C for 24 h, producing GO@APTES@DCDA.[43] Finally, the composite is coordinated with various metal ions (M^{n+} = Ni^{2+}, Co^{2+}, Zr^{4+}, Zn^{2+}, Al^{3+}, Fe^{3+}, Cr^{3+}, Sb^{3+}) in ethanol at 80 °C for 12 h,[44] resulting in the final product GO@APTES@DCDA@M^{n+}. The structure and surface chemistry of GO@APTES@DCDA@M^{n+} materials were determined through Fourier transform infrared spectroscopy (FT-IR), Raman spectroscopy, X-ray diffraction (XRD), scanning electron microscopy (SEM), energy-dispersive X-ray spectroscopy (EDX), inductively coupled plasma mass spectrometry (ICP-MS), X-ray photoelectron spectroscopy (XPS).

The FT-IR spectra presented in Fig. 1 provides valuable insights into the sequential functionalization of graphite, progressing through oxidation, salinization, amination, and coordination with Sb^{3+} ions. Each step produced characteristic vibrational bands, confirming the chemical modifications.

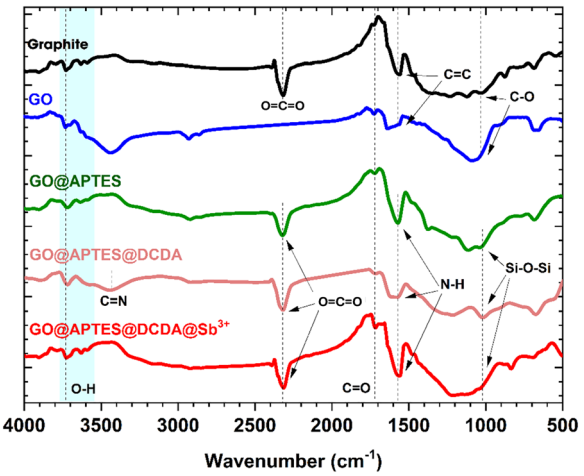

Fig. 1 FT-IR spectra of graphite, GO, GO@APTES, GO@APTES@DCDA, and GO@APTES@DCDA@Sb^{3+}.

The spectrum of pristine graphite exhibited a weak and broad absorption band around 1580 cm^{-1}, corresponding to C=C stretching vibrations in the aromatic lattice.[45,46] This observation is characteristic of the graphitic structure with minimal surface functional groups. Upon oxidation of GO, a significant increase in surface functionalities was observed. Notably, strong bands appeared near 1720 cm^{-1} and 1220 cm^{-1}, which were assigned to the stretching vibrations of C=O and C–O, respectively.[47] Additionally, a broad absorption band around 3400 cm^{-1} indicated the presence of hydroxyl groups, supporting the successful incorporation of oxygen-containing

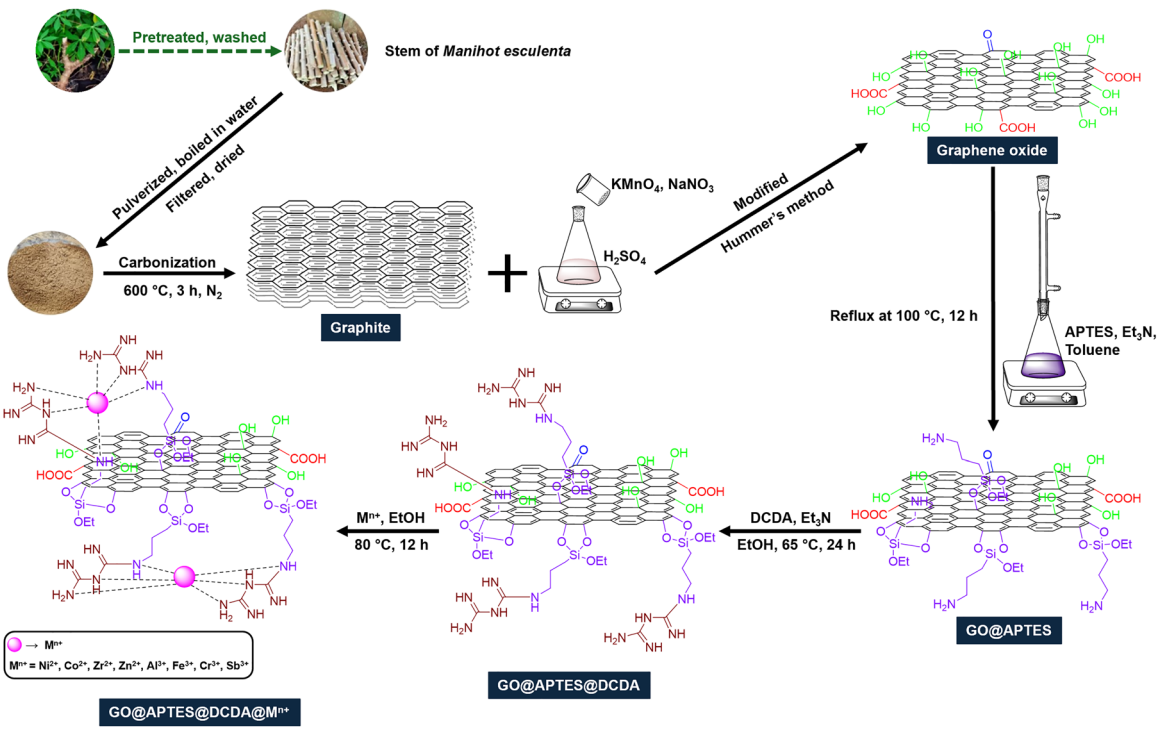

Scheme 2 Procedure for the synthesis of GO@APTES@DCDA@M^{n+}.

moieties.[48] Following salinization with APTES (GO@APTES), new bands emerged in the 1080–1150 cm^{-1} region, attributed to Si–O–Si symmetric and asymmetric stretching vibrations.[49] The results confirmed the successfully synthesis of GO@APTES, which confirmed the successful grafting of silane functionalities onto the GO surface. Concurrently, a reduction in the intensity of the C=O band suggested partial consumption or masking of carbonyl groups during the salinization process. Subsequent functionalization with dicyandiamide resulted in the appearance of distinct peaks around 1650 cm^{-1} and 1560 cm^{-1}, corresponding to C=N and N–H bending vibrations, respectively.[50] These results indicate the incorporation of nitrogen groups, probably through condensation or hydrogen bonding with surface groups. The presence of the C=N bond also suggested the introduction of conjugated nitrogen structures, which could influence the electronic properties of the material.[51] Coordination with Sb^{3+} ions (GO@APTES@DCDA@Sb^{3+}) led to subtle shifts in the C=O and C=N stretching bands, as well as increased intensity in the 1400–1700 cm^{-1} region. These changes reflected alterations in electron density distribution due to metal–ligand interactions. Minor variations in the Si–O–Si and N–H regions further indicated structural rearrangements upon Sb^{3+} complexation.[52] The persistent and broad O–H stretching band near 3400 cm^{-1} implied the retention of surface hydroxyl groups, which may contribute to enhanced metal coordination and catalytic stability.

The energy-dispersive X-ray (EDX) spectra illustrated in Fig. 2 further corroborates the sequential chemical functionalization and elemental composition of the produced materials. The spectrum of virgin graphite exhibited prominent peaks for carbon (C) alongside a small signal for oxygen (O), aligning with its highly graphitized structure and minimal surface oxidation. Minimal quantities of silicon (Si) and chlorine (Cl), presumably resulting from substrate or ambient contamination, were detected at low intensities. Oxidation to graphene oxide (GO) resulted in a significant increase in the oxygen signal, confirming the efficient incorporation of oxygen-containing functional groups, including hydroxyl, epoxy, and carboxyl moieties. The carbon-to-oxygen ratio markedly diminished relative to pristine graphite, characteristic of oxidized graphene derivatives. Nitrogen (N) was detected in trace quantities, perhaps resulting from little contamination or inadequate washing during synthesis. The salinization of GO using APTES (GO@APTES) was validated by a significant enhancement in the silicon signal, signifying the effective attachment of silane groups to the GO surface. The nitrogen level rose, indicating the incorporation of amine functions from the APTES molecule. These discoveries align with FTIR studies, which exhibited Si–O–Si and N–H stretching bands. The concurrent presence of Cl may be ascribed to the hydrolysis byproducts or counterions resulting from the salinization process. The further alteration with dicyandiamide (GO@APTES@DCDA) resulted in an increased nitrogen content, confirming the integration of nitrogen-rich groups such as C=N and N–H onto the functionalized GO. The comparative intensities of silicon and chlorine indicated that the DCDA alteration did not influence the silane moieties but instead engaged with the accessible surface functions. The conclusive coordination with antimony ions (GO@APTES@DCDA@Sb^{3+}) was distinctly shown by the appearance of specific Sb peaks at approximately 3.6 keV, 3.9 keV, and 4.1 keV. The detection of several Sb signals validated the effective immobilization of Sb^{3+} onto the modified GO matrix. The retention of nitrogen and silicon signals indicates that coordination transpired without considerable disturbance to previously grafted functions. The elemental analysis indicates that the material contains N, Si, and Sb, showing successful surface modification for catalytic

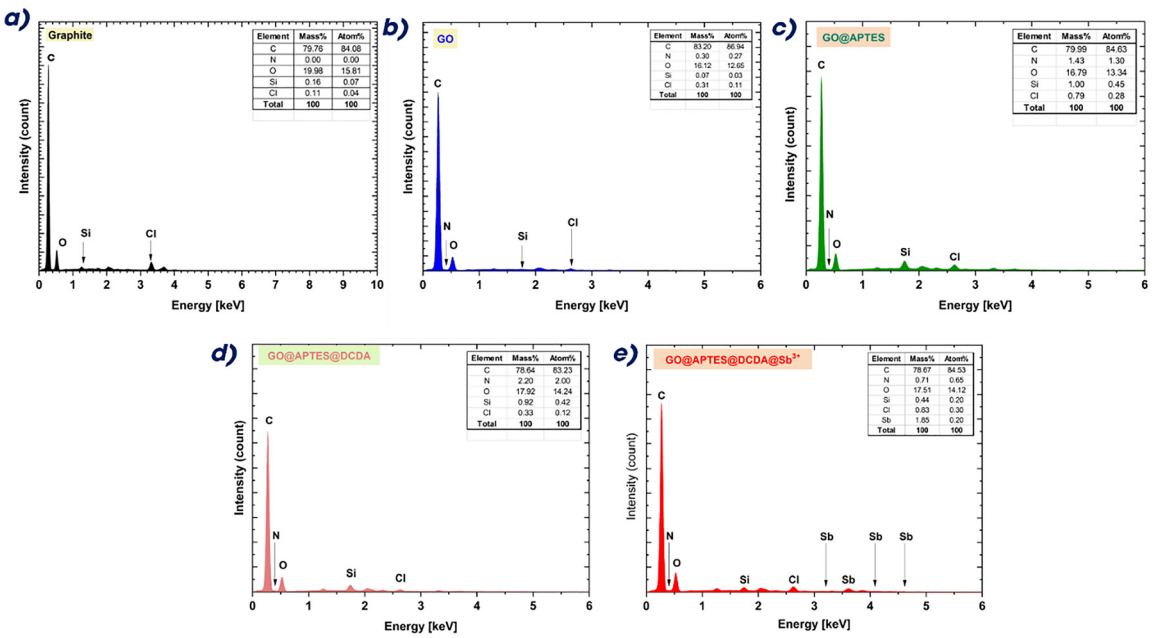

Fig. 2 EDX spectra of graphite (a), GO (b), GO@APTES (c), GO@APTES@DCDA (d), and GO@APTES@DCDA@Sb^{3+} (e).

use. The EDX analysis confirms the deliberate and systematic progression of elemental composition at each synthetic stage. The gradual integration of heteroatoms, especially nitrogen and antimony, is anticipated to improve the catalytic performance and electronic properties of the material.

The EDX elemental mapping presented in Fig. 3 provided compelling evidence for the successful stepwise modification of the GO-based catalyst. Pristine graphite (Fig. 3a) showed uniform distribution of carbon with minimal presence of oxygen, consistent with its unoxidized state. Upon oxidation to GO (Fig. 3b), oxygen content increased significantly, and the C and O signals were homogeneously dispersed, confirming the introduction of oxygen-containing functional groups across the graphene surface. In the GO@APTES sample (Fig. 3c), the presence of silicon was clearly detected, verifying the successful grafting of APTES molecules *via* silane chemistry. This was accompanied by a consistent distribution of nitrogen, indicating the introduction of amino functional groups. When DCDA

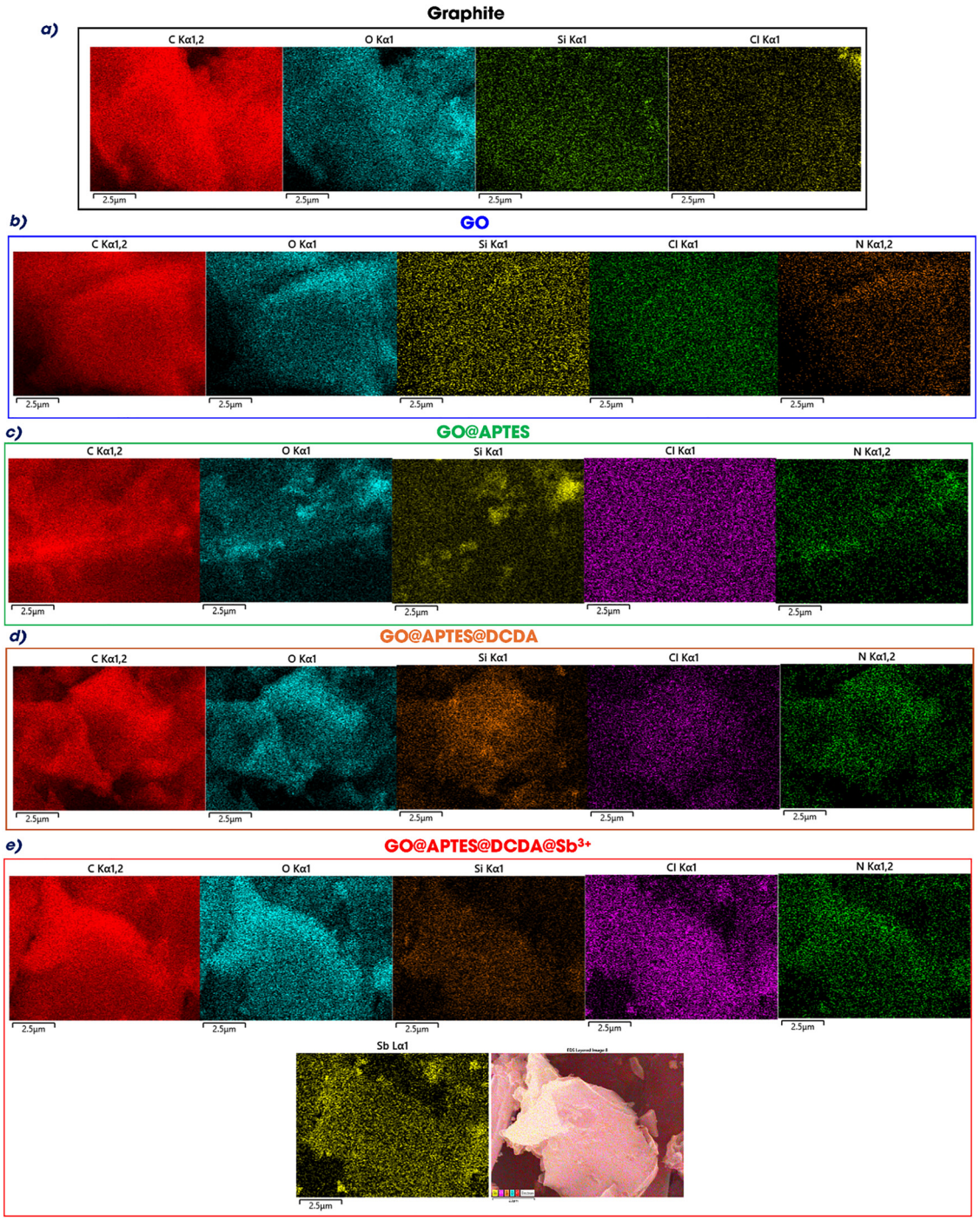

Fig. 3 EDX mapping of graphite (a), GO (b), GO@APTES (c), GO@APTES@DCDA (d), and GO@APTES@DCDA@Sb^{3+} (e).

was further incorporated to form GO@APTES@DCDA (Fig. 3d), the nitrogen signals intensified and spread more uniformly, supporting the enhancement of nitrogen doping due to DCDA polymerization, which is known to generate nitrogen-rich carbonaceous structures. The GO@APTES@DCDA@Sb^{3+} sample (Fig. 3e) exhibited a distinct signal corresponding to antimony, which was evenly distributed throughout the carbon matrix. This uniform dispersion suggested effective coordination of Sb^{3+} ions with nitrogen and oxygen functional groups on the support surface. The co-localization of C, N, O, and Sb elements highlighted the successful anchoring of antimony species within the doped framework.

The XRD patterns provided valuable information regarding the structural evolution of the catalyst at different synthesis stages (Fig. 4). The graphite sample showed a sharp and intense peak at around 26.5°, corresponding to the (002) plane, which is characteristic of the well-ordered crystalline structure of graphite.[53] Upon oxidation to graphene oxide (GO), this peak shifted to approximately 11.2°, indicating the formation of the (001) plane due to the insertion of oxygen-containing functional groups and the increase in interlayer spacing.[54] After functionalization with APTES, the GO@APTES sample exhibited a broader and less intense (001) peak, suggesting a partial reduction of GO and successful surface modification with silane groups. The introduction of DCDA in GO@APTES@DCDA further altered the structure, as seen by the slight changes in the diffraction pattern, indicating increased disorder and possible formation of nitrogen-containing domains within the GO matrix. The most complex structure, GO@APTES@DCDA@Sb^{3+}, showed additional sharp peaks corresponding to various crystalline planes, such as (003), (012), (104), (110), and others, confirming the incorporation of antimony species into the matrix.[55] These peaks matched well with crystalline Sb-based compounds, suggesting that Sb^{3+} was successfully coordinated or embedded within the composite. The reduction in GO-related peaks and emergence of Sb-associated signals confirmed the structural transformation

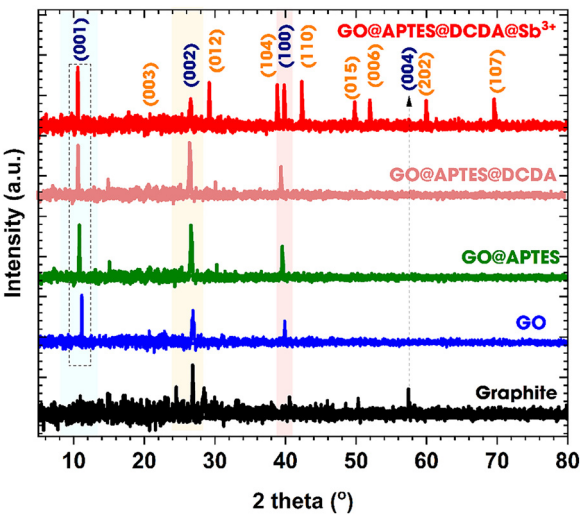

Fig. 4 XRD pattern of graphite, GO, GO@APTES, GO@APTES@DCDA, and GO@APTES@DCDA@Sb^{3+}.

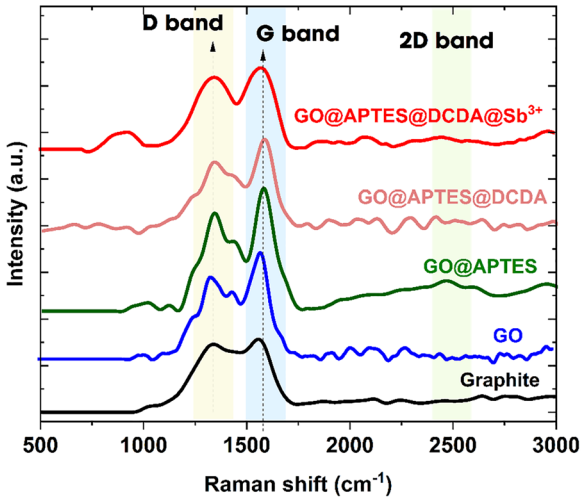

Fig. 5 Raman spectra of graphite, GO, GO@APTES, GO@APTES@DCDA, and GO@APTES@DCDA@Sb^{3+}.

from amorphous GO-based materials to a more crystalline, metal-containing catalyst. This evolution in crystallinity and peak profile provided strong evidence of successful multi-step functionalization and metal integration into the GO framework.

Fig. 5 presented the Raman spectra of graphite, GO, GO@APTES, GO@APTES@DCDA, and GO@APTES@DCDA@Sb^{3+}, offering crucial insights into the structural evolution of the catalyst materials. The pristine graphite showed a characteristic sharp G band around 1580 cm^{-1}, corresponding to the E_{2g} mode of sp^2-hybridized carbon atoms in a well-ordered graphitic lattice, and a negligible D band, indicating low defect density.[56] Upon oxidation to GO, the intensity of the D band ($\sim$1350 cm^{-1}) significantly increased, reflecting the introduction of defects and disordered sp^3 domains due to oxygenated functional groups. The I_D/I_G ratio notably rose, confirming structural disruption.[57] Subsequent surface functionalization with APTES led to further enhancement of the D band intensity in the GO@APTES sample, implying additional defects introduced by silane grafting and possible changes in π–π conjugation.[58] Incorporation of DCDA resulted in a more pronounced D band, suggesting nitrogen doping and further edge distortion, consistent with N-doped carbon framework formation. The final catalyst, GO@APTES@DCDA@Sb^{3+}, exhibited the highest D band intensity among all samples, with a significantly elevated I_D/I_G ratio. This indicated substantial disorder, likely due to the synergistic effects of N-doping and Sb^{3+} coordination, which disrupted the carbon lattice further but also potentially introduced catalytically active sites.

The Raman spectroscopy data in Table 1 elucidated the structural disorder and extent of graphitization in the catalyst samples *via* the intensity ratio of the D band to the G band (I_D/I_G). Pristine graphite demonstrated an I_D/I_G ratio of 0.93, indicating its reasonably organized sp^2-carbon lattice with few imperfections. Upon oxidation to GO, the I_D/I_G ratio diminished to 0.77, signifying that the incorporation of oxygenated functional groups disrupted the conjugated π-system while partially reinstating graphitic order through the development

Table 1 I_D/I_G ratio of graphite, GO, GO@APTES, GO@APTES@DCDA, and GO@APTES@DCDA@Sb^{3+}

Sample name	D band	G band	I_D/I_G
Graphite	145.08	156.52	0.93
GO	116.28	150.57	0.77
GO@APTES	182.52	228.36	0.80
GO@APTES@DCDA	140.58	197.17	0.71
GO@APTES@DCDA@Sb^{3+}	135.61	140.26	0.97

of smaller sp^2 domains within the oxidized matrix.[59] After surface functionalization with APTES, the I_D/I_G ratio increased marginally to 0.80, indicating a minor increase in structural flaws resulting from the covalent attachment of silane molecules to the GO surface. Upon further modification of GO@APTES with DCDA, the I_D/I_G ratio diminished to 0.71, suggesting a partial restoration of graphitic domains, possibly facilitated by heat treatment and nitrogen doping, which enhanced electronic conjugation. The ultimate integration of Sb^{3+} into GO@APTES@DCDA markedly elevated the I_D/I_G ratio to 0.97, the highest recorded among all samples. The significant increase indicated that the introduction of antimony ions caused considerable structural deformation, likely due to the coordination of Sb^{3+} with nitrogen or oxygen functions, which further disturbed the carbon framework. The rise in defect density was likely advantageous for catalytic applications, as it may have augmented the quantity of active sites and enhanced catalytic performance.

Fig. 6 presented the SEM pictures of graphite, GO, GO@APTES, GO@APTES@DCDA, and GO@APTES@DCDA@Sb^{3+}, illustrating the morphological progression throughout the synthesis stages. Pristine graphite exhibited a smooth, layered lamellar structure, indicative of densely arranged graphene layers. Upon oxidation to GO, the layers exhibited more exfoliation, characterized by an augmented interlayer distance and enhanced surface roughness, indicative of the successful incorporation of oxygen-containing functional groups and the breakage of π–π stacking interactions.[60] The functionalization with APTES led to additional delamination and the emergence of uneven surface textures in the GO@APTES sample. These characteristics suggested silane grafting and the partial degradation of the sheet-like structure, hence increasing the surface area and possible interaction sites. The integration of DCDA resulted in the GO@APTES@DCDA material displaying a more convoluted and porous architecture, indicating that nitrogen doping and heat processing induced microstructural disorder and porosity pathways advantageous for catalytic applications. The SEM images of GO@APTES@DCDA@Sb^{3+} exhibited a notable alteration, characterized by broken, crumpled flakes and distributed aggregates. The surface exhibited significant irregularity and roughness, suggesting that Sb^{3+} coordination

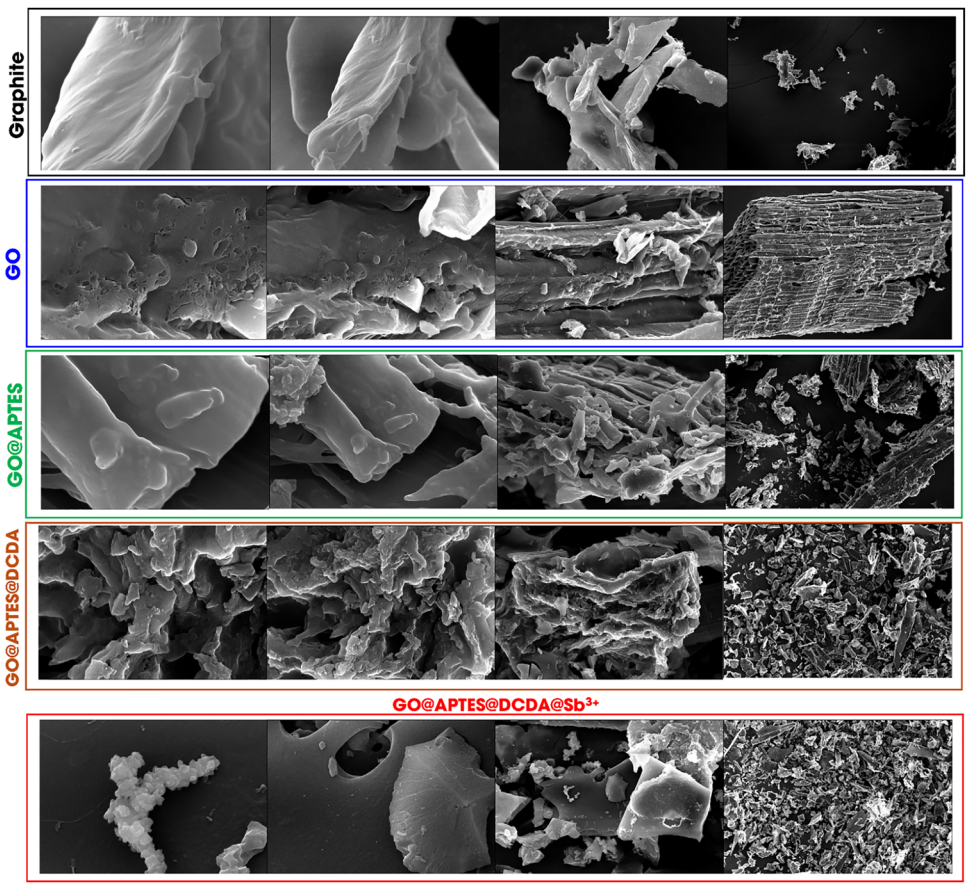

Fig. 6 SEM images of graphite, GO, GO@APTES, GO@APTES@DCDA, and GO@APTES@DCDA@Sb^{3+}.

altered the morphology and prompted nanoscale remodeling, potentially *via* metal–ligand complexation or precipitation phenomena. Inductively coupled plasma mass spectrometry (ICP-MS) determined that the amount of element Sb present in the GO@APTES@DCDA@Sb^{3+} catalyst was 8.20 mmol g^{-1}.

X-ray photoelectron spectroscopy (XPS) was employed to explore the elemental composition and chemical states of the synthesized catalyst, as shown in Fig. 7. The survey spectrum (Fig. 7a) confirmed the presence of key elements, including carbon (C), nitrogen (N), oxygen (O), silicon (Si), and antimony (Sb), each contributing distinct peaks within the binding energy range. In the C 1s region (Fig. 7b), four distinct binding-energy peaks were observed at 284.2, 285.5, 287.7, and 292.7 eV, which are associated with different carbon bonding environments. The peak at 284.2 eV is attributed to the C–C/C=C bonding in the carbonaceous backbone, typical for graphitic or sp^2 hybridized carbon. The peak at 285.5 eV corresponds to C–N bonds, indicating the presence of nitrogen-functionalized carbon species within the catalyst. The peak at 287.7 eV is related to C=O bonding, suggesting the presence of carbonyl groups or other oxygenated functionalities on the surface. Finally, the peak at 292.7 eV corresponds to the π–π satellite* transitions, indicative of conjugated carbon networks or aromatic systems, which may suggest delocalized electrons in the carbon-rich surface regions. These findings confirm the presence of oxygenated and nitrogenated carbon functionalities, which are significant for catalytic activity.[61,62] In the N 1s region (Fig. 7e), the spectrum shows a broad peak that was deconvoluted into three components, located at 398.9, 399.7, and 401.1 eV. The peak at 398.9 eV is assigned to nitrogen in the C–N environment, indicating the presence of amines or imines in the catalyst structure. The peak at 399.7 eV is associated with C=N bonds, suggesting the presence of imine groups, while the peak at 401.1 eV corresponds to C–NH_2 groups, indicative of primary amine functionalization on the surface. These nitrogen-containing groups are often involved in catalytic processes, particularly in reactions that require electron donation or surface coordination with metal centers.[61] The Sb 3d and O 1s regions provide further insights into the nature of the catalyst's surface. In the Sb 3d region (Fig. 7d), two prominent peaks were observed at 539.1 and 530.0 eV, which correspond to the Sb $3d_{3/2}$ and Sb $3d_{5/2}$ states, respectively. These peaks are characteristic of antimony, confirming its presence in the catalyst. The precise nature of these peaks suggests that antimony may be incorporated into the catalyst either in an oxidized form Sb(III) or Sb(V). The O 1s region (Fig. 7a) revealed two key contributions at 531.6 and 532.8 eV, which can be attributed to C=O and Si–O bonding, respectively. The peak at 531.6 eV corresponds to oxygen in carbonyl groups or other forms of surface-bound oxygen, while the peak at 532.8 eV is associated with Si–O bonds, indicating the presence of silicate or siloxane groups, which are typical in hybrid materials where silicon is coordinated with oxygen.[63,64] The Si 2p region (Fig. 7c) showed peaks at 97.7, 102.0, and 101.6 eV. The peak at 97.7 eV is attributed to Si $2p_{3/2}$, which is typical for silicon in a silicon oxide (SiO_2) environment. The peak at 102.0 eV corresponds to Si–O–C bonding, indicating that silicon is covalently bonded to carbon through oxygen, which is common in hybrid organic–inorganic materials. The peak at 101.6 eV is assigned to Si $2p_{1/2}$, confirming the presence of silicon in the structure.[64,65]

2.2. Catalytic activity of GO@APTES@DCDA@Sb^{3+}

The activity of GO@APTES@DCDA@Sb^{3+} was evaluated through a one-pot multicomponent cyclization reaction between aniline (2 mmol), benzaldehyde (2 mmol), and ethyl acetoacetate

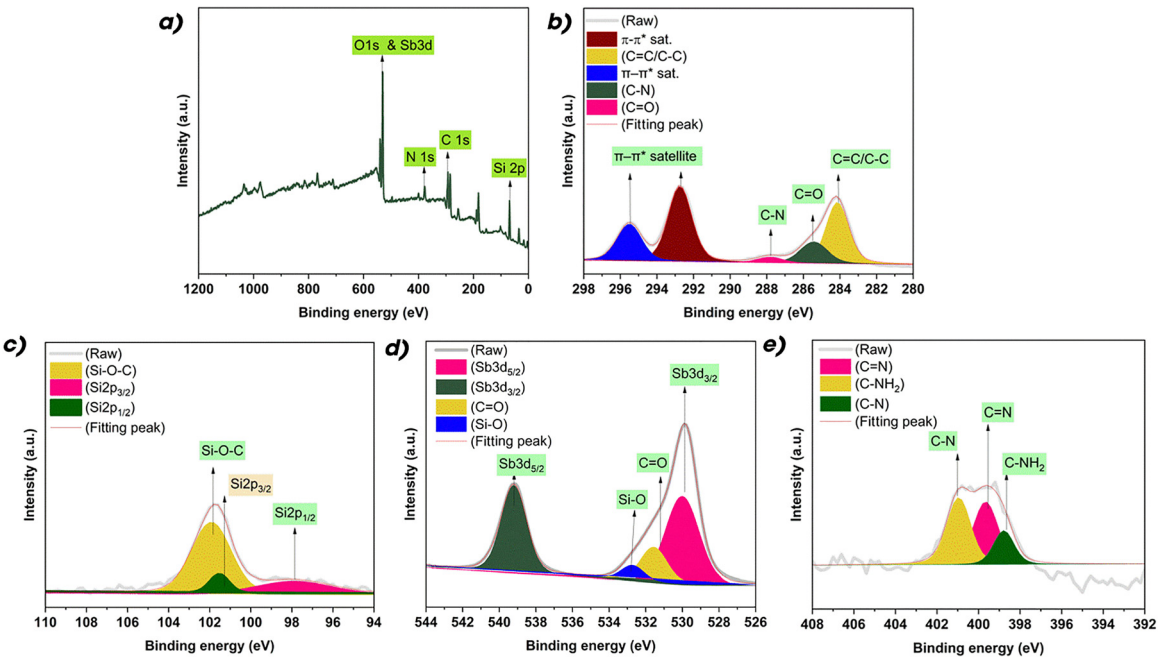

Fig. 7 XPS analysis of GO@APTES@DCDA@Sb^{3+} catalyst with (a) survey XPS spectra, high-resolution XPS spectra of (b) C 1s, (c) Si 2p, (d) Sb 3d, and (e) N 1s.

(1 mmol) to afford ethyl 1,2,6-triphenyl-4-(phenylamino)-1,2,5,6-tetrahydropyridine-3-carboxylate (**4a**) (Scheme 3).

The catalytic performance strongly depends on the type of catalyst employed, as summarized in Table 2. In the absence of a catalyst or when using pristine graphite and GO, the reaction afforded only low yields (20–23%), indicating their limited intrinsic catalytic activity (entries 1–3, Table 2). Functionalization of GO with APTES and DCDA did not significantly improve the outcome, with yields remaining around 22–23% (entries 4–5, Table 2). Upon incorporation of metal species into the GO@APTES@DCDA framework, both yield and diastereoselectivity (*syn* : *anti*) became strongly metal-dependent. For example, Ni^{2+} and Co^{2+} provided modest yields (20–21%) with moderate *anti* selectivity (13 : 87 and 8 : 92, respectively; entries 6–7, Table 2), while Zr^{4+} and Fe^{3+} improved the yield to 26% and 25%, respectively, but showed pronounced *anti* selectivity (3 : 97; entries 8 and 11, Table 2). Cr^{3+} afforded 21% yield with 18 : 82 *syn* : *anti* ratio (entry 12, Table 2). Notably, the Sb^{3+}-modified catalyst exhibited the highest activity (56% yield) with a *syn* : *anti* ratio of 8 : 92 (entry 13, Table 2), indicating both enhanced efficiency and good diastereocontrol toward the *anti* isomer. In contrast, Al^{3+} gave a lower yield (14%) and 5 : 95 selectivity (entry 10, Table 2), highlighting that both reactivity and stereochemical outcome are highly sensitive to the nature of the incorporated metal. A comparison with simple metal salts further underscores this effect. Although $SbCl_3$ and $CoCl_2$ showed moderate yields (36% and 35%, respectively), their *syn* : *anti* ratios (3 : 97 and 1 : 99; entries 21 and 15, Table 2) indicate high *anti* selectivity but lower overall efficiency compared to the supported GO@APTES@DCDA@Sb^{3+} catalyst. Other salts such as $ZnCl_2$ (25%, 22 : 78) and $FeCl_3$ (22%, 19 : 81) displayed variable selectivities, while $ZrOCl_2$ gave only 10% yield despite strong *anti* preference (1 : 99; entry 16, Table 2). These results demonstrate that the synergy between the GO-based framework and Sb^{3+} centers not only enhances catalytic activity but also maintains favorable *anti* diastereoselectivity. The reaction was almost non-existent under microwave irradiation for 15 min (entry 13, Table 2), confirming that prolonged conventional heating is required for efficient transformation.

Table S1 examines the influence of multiple reaction parameters including time, temperature, solvents, and catalyst loading on the isolated yield of (**4a**), synthesized *via* a multicomponent reaction catalyzed by GO@APTES@DCDA@Sb^{3+}. The experiments were conducted under a consistent substrate ratio (benzaldehyde : aniline : ethyl acetoacetate = 1 : 1 : 0.5) and

Table 2 The impact of various types of GO@APTES@DCDA@M^{n+} and corresponding metal halides on the yield of (**4a**)[a]

Entry	Catalysts	Isolated yield[b] (**4a**) (%)	Ratio of *syn* : *anti*[c]
1	None	23	29 : 71
2	Graphite	20	26 : 74
3	GO	20	37 : 63
4	GO@APTES	22	4 : 96
5	GO@APTES@DCDA	23	14 : 86
6	GO@APTES@DCDA@Ni^{2+}	21	13 : 87
7	GO@APTES@DCDA@Co^{2+}	20	8 : 92
8	GO@APTES@DCDA@Zr^{4+}	26	3 : 97
9	GO@APTES@DCDA@Zn^{2+}	23	2 : 98
10	GO@APTES@DCDA@Al^{3+}	14	5 : 95
11	GO@APTES@DCDA@Fe^{3+}	25	3 : 97
12	GO@APTES@DCDA@Cr^{3+}	21	18 : 82
13	**GO@APTES@DCDA@Sb^{3+}**	**56 (3)[d]**	**8 : 92**
14	$NiCl_2{\cdot}6H_2O$	27	3 : 97
15	$CoCl_2{\cdot}6H_2O$	35	1 : 99
16	$ZrOCl_2{\cdot}8H_2O$	10	1 : 99
17	$ZnCl_2$	25	22 : 78
18	$AlCl_3$	24	14 : 86
19	$FeCl_3{\cdot}6H_2O$	22	19 : 81
20	$CrCl_3{\cdot}6H_2O$	30	3 : 97
21	$SbCl_3$	36	3 : 97

[a] Reaction conditions: benzaldehyde (1 mmol), aniline (1 mmol), ethyl acetoacetate (0.5 mmol) and catalysts (5 mg) under solvent-free at 50 °C for 380 min. [b] Isolated yield by crystallization in ethanol (10 mL). [c] HPLC. [d] Microwave irradiation: 80 W, 15 min.

fixed catalyst structure, allowing for a focused interpretation of individual parameter effects. Reaction time plays an important role in the yield of the reaction.[66] The reaction was monitored across a wide range of durations (90–750 minutes), with the resulting yield profile revealing significant insights into the kinetics and limitations of the multicomponent condensation process (entries 1–17, Table S1). At reduced reaction times, namely from 90 to 270 minutes, the production of (**4a**) is minimal, with yields varying from 0 to merely 2% (entries 6–9, Table S1). This suggests that the reaction progresses slowly in the initial phases, probably because of the time needed for the sequential synthesis of imine and enamine intermediates and their ensuing cyclization. The poor initial conversion indicates that the process is kinetically regulated, necessitating prolonged thermal input to attain significant transformation. As the reaction time escalates from 330 to 380 min, a substantial increase in yield is noted, culminating at 56% at 380 min (entries 2 and 10, Table S1). This signifies the ideal reaction period, allowing ample time for all reactions to participate in the multistep condensation under catalysis, while ensuring good selectivity and few side reactions. This state signifies the

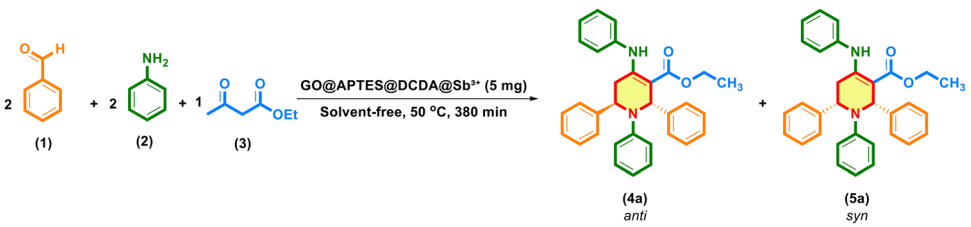

Scheme 3 Synthesis of ethyl 1,2,6-triphenyl-4-(phenylamino)-1,2,5,6-tetrahydropyridine-3-carboxylate.

system's kinetic maximum, beyond which declining returns occur. Exceeding 380 min, the findings indicate a modest although distinct decrease in yield with extended reaction durations (entries 3–5 and 11–17, Table S1). Yields are moderate at 390–450 minutes, which accounted for about 35%, while extending to 510–570 min sustains the yield at 36%, indicating the system achieves a dynamic equilibrium or steady state (entries 3 and 12–14, Table S1). Extending the reaction beyond this duration leads to a significant decrease in yield falling to 25% at 630 min and achieving at about 11% by 750 min (entries 15 and 17, Table S1). The decrease in yield may result from product degradation during extended heating, partial deactivation of the catalyst, or the formation of undesired byproducts. The reaction profile demonstrates that a crucial duration of 380 min is essential for optimizing yield under the specified conditions. Inadequate periods hinder complete conversion, whereas prolonged exposure results in competitive side effects and product instability. These findings underscore the significance of time as a critical factor in heterogeneous catalysis, particularly for multicomponent systems that encompass sequential and reversible processes. The results indicate a clear relationship between temperature and catalytic efficiency, highlighting the temperature sensitivity of this multicomponent reaction. At room temperature, the reaction produces merely 19%, suggesting that ambient thermal energy is inadequate to surmount the activation barriers linked to the sequential formation of critical intermediates, such as the imine and enamine species, along with the final cyclization step (entry 18, Table S1). This suboptimal performance underscores the requirement for extra thermal energy to propel the reaction to completion. Raising the reaction temperature to 60 °C markedly enhances the yield to 41%, attributable to the accelerated rates of condensation and ring-closure processes (entry 19, Table S1). The temperature seems nearly perfect, since increasing it to 70 °C and 80 °C results in only marginal increases in product creation, yielding 39% and 40%, respectively (entries 20 and 21, Table S1). At higher temperatures, the yield did not improve further, probably because of side reactions or partial decomposition of intermediates. The reaction yield was approximately 56% at 50 °C (entry 2, Table S1). Fundamentally, these findings indicate that moderate heating (50–80 °C) markedly enhances the reaction compared to ambient temperatures, although no considerable advantage is achieved above 50 °C. Consequently, 50 °C signifies the optimal energy-efficient condition, yielding a high output while avoiding the concerns of thermal degradation and excessive energy expenditure. Of the solvents evaluated, only dichloromethane produced a substantial yield with 37%, which is remarkable given that all other solvents yielded either negligible or trace amounts of product (entry 32, Table S1). This observation indicates that the reaction milieu offered by dichloromethane characterized as a moderate polar, aprotic, and low-boiling organic solvent promotes the formation and stabilization of reactive intermediates, such as imine and enamine species, and aids the ensuing cyclization step that yields the final piperidine product. Conversely, the yield of the reaction was reached at about 6%, 13%, and 9% when using protic solvents including water, methanol, ethanol, respectively, which produced far lower conversions (entries 22–24, Table S1). This can be ascribed to the competitive hydrogen bonding and solvation of crucial intermediates, which may obstruct the nucleophilic attack required for cyclization. Moreover, these solvents may facilitate the hydrolysis of reactive intermediates, so redirecting the reaction from the intended pathway. Alcohols such as 2-propanol and 1-butanol exhibited only trace quantities of product, presumably due to their heightened steric hindrance and diminished polarity, which further obstructs the catalytic cycle (entries 25 and 26, Table S1). Notably, polar aprotic solvents like DMF, DMSO, acetonitrile, and THF did not facilitate substantial product formation (entries 29–31 and 33, Table S1). Although these solvents often stabilize charged intermediates in numerous chemical processes, their potent solvation capacity may disrupt essential hydrogen-bonding interactions or catalyst–substrate connections vital for the efficacy of this multicomponent condensation. Comparable trace results were seen for prevalent chlorinated solvents, including chloroform and 1,4-dioxane, as well as for non-polar solvents including hexane and toluene, underscoring the necessity for a meticulously calibrated solvent environment (entries 35 and 37–39, Table S1). A significant observation is that the ethanol:water binary system yielded only trace amounts, suggesting that the simple amalgamation of individual solvent components with moderate efficacy does not ensure synergistic improvement, likely attributable to phase behavior or adverse solvation dynamics in the mixed medium (entry 27, Table S1). Among the solvents tested, the catalyst performed best under solvent-free conditions for piperidine synthesis. The effect of catalyst loading was investigated between 1 and 20 mg (entries 40–46, Table S1). A significant rise in yield is observed from 29% (1 mg) to a maximum of 56% at 5 mg, confirming the necessity of sufficient catalytic surface area for effective transformation (entry 2, Table S1). However, further increase in catalyst amount does not lead to improved performance and instead results in diminished yields. For example, the yield of reaction reached about 33% at 20 mg (entry 46, Table S1).

Table 3 provides a systematic assessment of the impact of different substrate ratios on the isolated yield of (**4a**) utilizing GO@APTES@DCDA@Sb^{3+} as the catalyst under consistent circumstances (50 °C, 380 minutes, 5 mg catalyst). The multicomponent reaction comprises benzaldehyde, aniline, and ethyl acetoacetate, with their molar ratios systematically modified to determine the ideal stoichiometry for enhancing product yield. The reaction rates of benzaldehyde (2 mmol), aniline (2 mmol) and ethyl acetoacetate (1 mmol) were recorded with the highest yield of product (**4a**) reaching 56% (entry 1, Table 3). An excess of benzaldehyde (2.5 mmol) compared to aniline (2 mmol) and ethyl acetoacetate (1 mmol) yields 21% (entry 2, Table 3). This comparatively poor conversion indicates that an excess of the aldehyde may result in competitive side reactions, such as self-condensation or excessive condensation with the amine, so undermining the effectiveness of the intended transformation. In contrast, increasing the aniline

Table 3 The impact of substrate ratio with GO@APTES@DCDA@Sb^{3+} as a catalyst[a]

	Substrate ratio (mmol)			
Entry	Benzaldehyde	Aniline	Ethyl acetoacetate	Isolated yield[b] (**4a**) (%)
1	**2**	**2**	**1**	**56**
2	2.5	2	1	21
3	2	2.5	1	15
4	2	2	1.5	24
5	2	2	2	27

[a] Reaction conditions: GO@APTES@DCDA@Sb^{3+} (5 mg) under solvent-free condition at 50 °C for 380 min. [b] Isolated yield by crystallization in ethanol (10 mL).

to 2.5 mmol while keeping lower equivalents of the other substrates results in just 15% yield of (**4a**) (entry 3, Table 3). This suggests that an excess of amine is detrimental to the reaction pathway, possibly due to imine oligomerization or inhibitory interactions with the Lewis acid catalyst, Sb^{3+}. A more advantageous result is noted, with ethyl acetoacetate increased to 1.5 mmol alongside equimolar amounts of benzaldehyde (2 mmol) and aniline (2 mmol), resulting in a yield of 24% (entry 4, Table 3). This enhancement indicates that the β-ketoester is essential in promoting the cyclization phase, and its scarcity becomes a limiting factor when insufficiently present. The optimal yield (27%) is attained with a balanced molar ratio of 2 : 2 : 2, signifying that stoichiometric equality among the three substrates provides the most effective conversion route under the specified reaction circumstances (entry 5, Table 3).

The optimization experiment for the GO : APTES ratio was conducted using the following conditions: 0.1 g of GO combined with 1, 1.5, and 2 mL of APTES (Table 4). After obtaining GO@APTES at each ratio, the subsequent steps were carried out according to the catalyst synthesis procedure described earlier. The resulting GO@APTES@DCDA@Sb^{3+} materials were then employed as catalysts in the model reaction between benzaldehyde, aniline and ethyl acetoacetate. The results clearly indicate that increasing the amount of APTES leads to a significant decline in catalytic performance. As the APTES volume increased from 1 to 1.5 mL, the reaction yield decreased from 56% to 33%. A further increase to 2 mL resulted in a drastic drop to only 16%. This trend suggests that excessive APTES grafting does not enhance, but rather inhibits, the catalytic activity of GO@APTES@DCDA@Sb^{3+}.

Table 4 The impact of various ratio of GO and APTES to form GO@APTES@DCDA@Sb^{3+} on the yield of (**4a**)[a]

	GO@APTES@DCDA@Sb^{3+} (5 mg)		
Entry	GO (g)	APTES (mL)	Isolated yield[b] (**4a**) (%)
1	**0.1**	**1**	**56**
2	0.1	1.5	33
3	0.1	2	16

[a] Reaction conditions: benzaldehyde (1 mmol), aniline (1 mmol), ethyl acetoacetate (0.5 mmol) and GO@APTES@DCDA@Sb^{3+} (5 mg) under solvent-free at 50 °C for 380 min. [b] Isolated yield by crystallization in ethanol (10 mL).

The one-pot multicomponent condensation reaction between arylaldehydes (**1**), arylamines (**2**), and ethyl acetoacetate (**3**) in the presence of GO@APTES@DCDA@Sb^{+} afforded 1,2,5,6-tetrahydropyridine-3-carboxylate derivatives under solvent-free conditions at 50 °C for 380 min (Scheme 4). The product distribution reveals that the *anti*-isomer (**4**) is strongly favored in most cases, as indicated by the *syn* : *anti* ratio of 0 : 100 for many substrates. Only in the cases of benzaldehyde derivatives with unsubstituted (**4a**), fluoro-substituted (**4b**), and chloro-substituted (**4c**) at the *para*-postion were mixtures of *syn* and *anti* observed, with ratios of 9 : 91, 4 : 96, and 0 : 100, respectively. This suggests that the absence of strong electronic effects, or the presence of weak electron-withdrawing groups, reduces stereocontrol during the cyclization step, allowing partial *syn* formation. The isolated yields vary significantly depending on the substituents on the aromatic aldehyde (**1**). The highest yield was obtained for the benzaldehyde (**4a**) (56%), while yields decreased in the presence of strongly electron-withdrawing groups at the *para* position such as –OMe (**4f**, 20%), and $-NO_2$ (**4g**, 21%). For benzaldehydes with halogen substituents at the *para* position (*e.g.*, –F, –Cl, –Br) the yields were 43% (**4b**), 43% (**4c**), 40% (**4d**), respectively. These substituents deactivate the aldehyde toward nucleophilic attack in the initial aza-Diels–Alder cyclization step, thereby lowering the efficiency of product formation. Similarly, bulky groups with multiple substituents –OMe (**4h**, 14%;) caused steric hindrance, resulting in reduced yields. For aniline derivatives bearing –Cl substituents at positions 3 and 5, the yield of the product reached 32% (*e.g.*, **4p**, 28%; **4q**, 32%, and **4r**, 16%). The catalytic activity of the synthesized derivatives of the 1,2,5,6-tetrahydropyridine-3-carboxylate was also determined from their TON and TOF criteria. The outcome revealed a significant difference in catalytic activity among the series of substrates used. The highest activity was reported for the compound **4a** with a TON and TOF value of 34 and 5 h^{-1}, respectively, showing elevated catalytic turnover with the optimized reaction conditions. Conversely, the lowest performance was documented for the compound **4h** (TON = 9, TOF = 1 h^{-1}), which signified low substrate activation. Most of the other derivatives demonstrated moderate catalytic activity, with TON values in the range of 17–26 and TOF values in the range of 3–4 h^{-1}, thereby confirming that the catalyst maintains its activity throughout the reaction cycles. The results emphasize that subtle electronic and steric variations in the substrates significantly influence the turnover behavior, and electron donors are generally favorable in raising the values of TON/TOF. In conclusion, the evidence supports that the catalytic system displays robustness, and shows tunability, in offering a promising platform for further optimization. Furthermore, we also investigated the aliphatic aldehyde, amine and other 1,3-diketones. Replacement of benzaldehyde with heptaldehyde did not afford the desired product, likely due to the lower stability and higher tendency of alphatic imines toward hydrolysis and side reactions compared with conjugation-stabilized aromatic imines. Similarly, substituting ethyl acetoacetate with acetylacetone failed, as 1,3-diketones were more acidic and generate overly

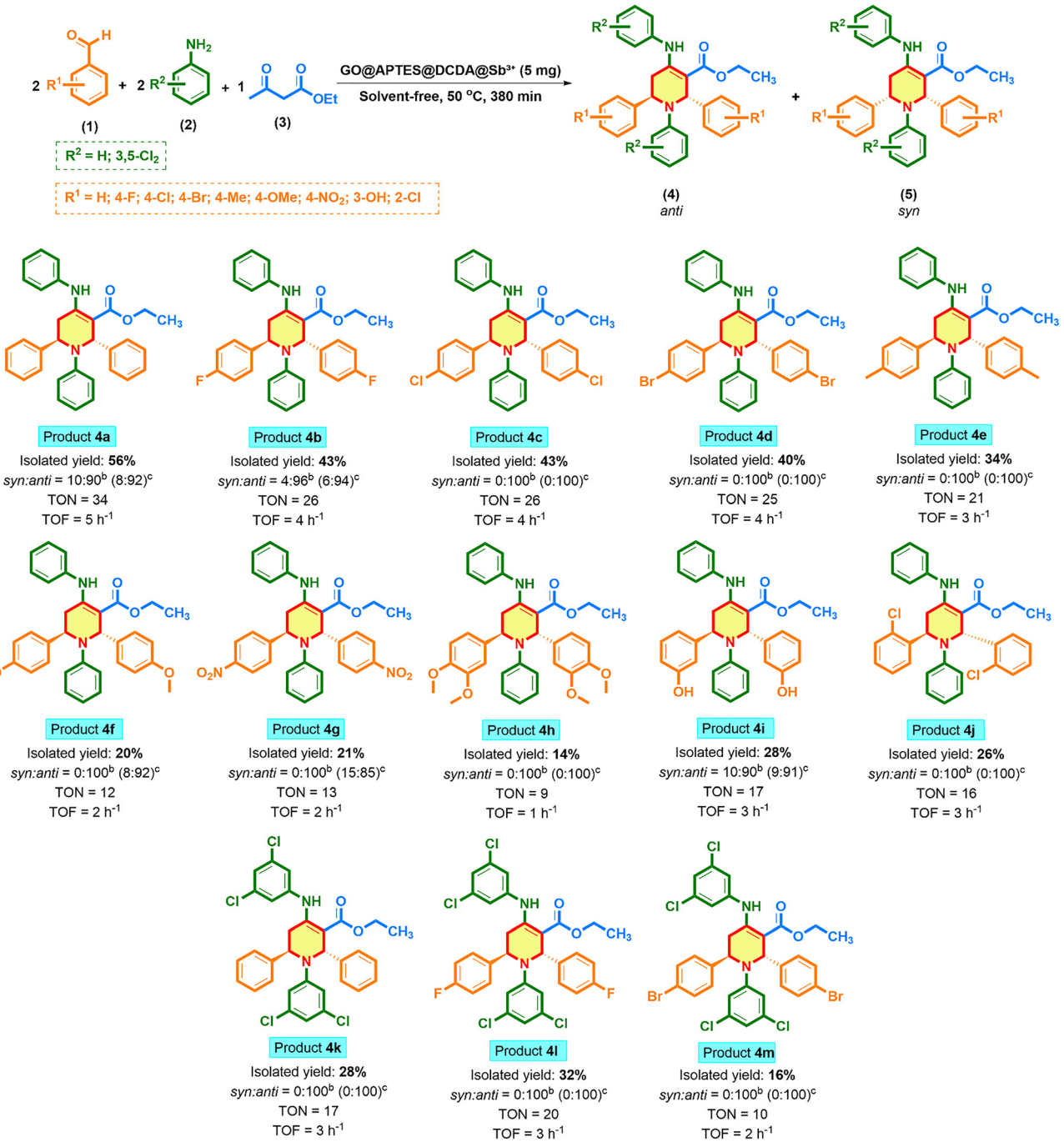

Scheme 4 Scope of 1,2,5,6-tetrahydropyridine-3-carboxylates.[a] [a]Reaction conditions: benzaldehyde derivatives (1 mmol), aniline derivatives (1 mmol), ethyl acetoacetate (0.5 mmol), GO@APTES@DCDA@Sb^{3+} (5 mg), solvent-free at 50 °C for 380 min. Isolated yield by crystallization in ethanol (10–15 mL). TON = (mole of products)/(mole of catalyst); TOF = TON/hour (h^{-1}). [b]The ratio of *syn* : *anti* was recorded as NMR. [c]The ratio of *syn* : *anti* was recorded as HPLC.

reactive enolates that often reduce selectivity and increase side reactions rather than productive cascade cyclization. Finally, substitution of aniline with hexylamine resulted in a similar failure, which was consistent with the lower stability of aliphatic imines and their greater tendency toward hydrolysis or undesired pathways compared with resonance-stabilized aromatic imines; analogous observations have been described in imine-mediated multicomponent reactions where aliphatic amines afford poor or no product.

2.3. Dynamic study

To elucidate the adsorption kinetics of the studied system, a series of time-dependent experiments were performed. The target compound, (2*S*,6*R*) ethyl 1,2,6-triphenyl-4-(phenylamino)-1,2,5,6-tetrahydropyridine-3-carboxylate (**4a**), was synthesized and prepared in a concentration of 10, 20, 50, 100, 200, 500, 100, and 2000 ppm. A calibration curve was subsequently established using HPLC-DAD analysis, as illustrated in Fig. 8. Adsorption aliquots were collected at

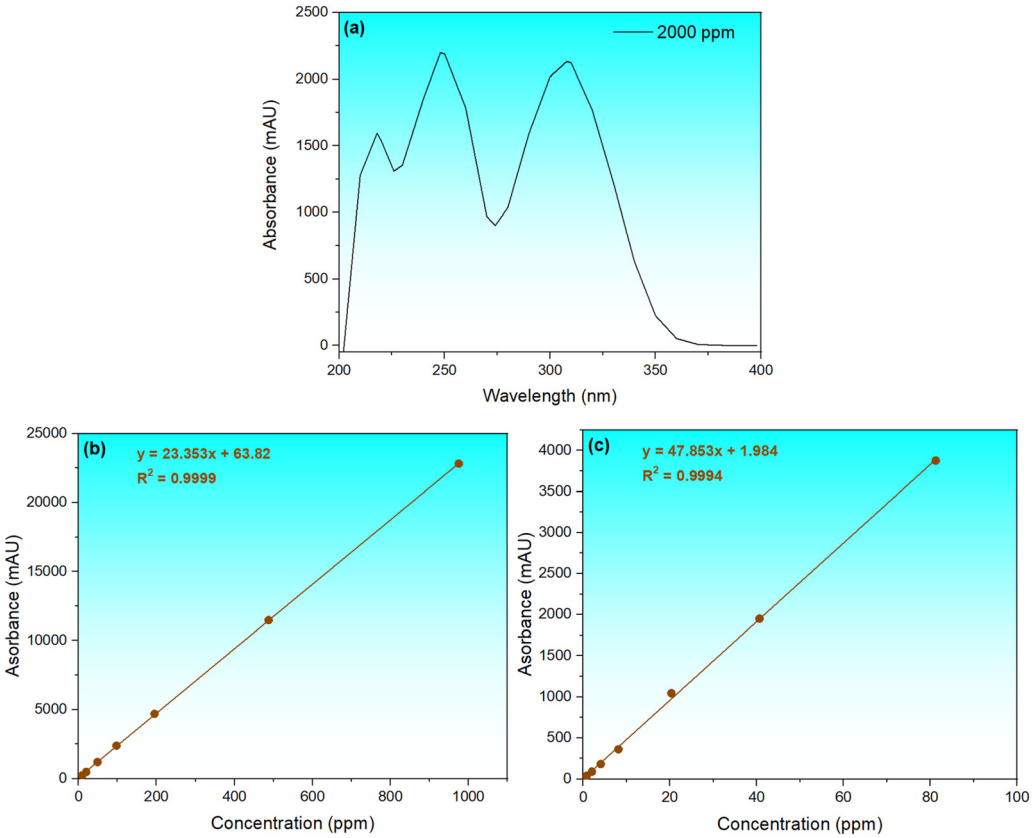

Fig. 8 (a) Absorbance of 100 ppm of ethyl 1,2,6-triphenyl-4-(phenylamino)-1,2,5,6-tetrahydropyridine-3-carboxylate (**4a**), (b) calibration curve (at λ = 305 nm) of *anti*-isomer (**4a**), (c) calibration curve (at λ = 305 nm) of *syn*-isomer (**4a**).

specific intervals of 3, 6, 15, 30, 60, 120, 180, 240, 300, 360, 480, and 540 min under isothermal conditions at 50, 60, and 80 °C. The resulting concentration data were utilized to determine the kinetic parameters and evaluate the kinetic model of the process.

To elucidate the governing mechanism of the interaction between the synthesized product (**4a**) and the GO@APTES@DCDA@Sb^{3+} catalyst surface, the experimental kinetic data were fitted using three classical models: pseudo-first order, pseudo-second order, and Elovich models.[67,68] The determination of adsorption kinetics at different temperatures is illustrated in Fig. 9, Fig. S1, Table 5, and Table S3, indicated that the pseudo-first order model provided an inadequate description of the system, characterized by relatively low values (*e.g.*, 0.8157 at 60 °C). Similarly, the Elovich model, which typically describes gas–solid adsorption on highly heterogeneous surfaces, did not show a high degree of correlation with the liquid-phase experimental data. In contrast, the pseudo-second order model exhibited superior fitting across all investigated temperatures (50, 60, and 80 °C), with values reaching to 0.9902.

The pseudo-second order adsorption kinetics of the product were analyzed using the linearized form of the model:[67,68]

$$\frac{t}{q_t} = \frac{1}{Kq_e^2} + \frac{t}{q_e}$$

where q_t (mg g^{-1}) is the amount of adsorbate adsorbed at time (t), q_e (mg g^{-1}) is the amount adsorbate adsorbed at equilibrium, and K (g mg^{-1} min^{-1}) is the pseudo-second order rate constant.

Furthermore, the calculated equilibrium adsorption capacities ($q_{e(cal)}$) of 281, 332, and 740 mg g^{-1} were in excellent agreement with the experimental values ($q_{e(exp)}$) of 268, 353, and 777 mg g^{-1}, respectively. This strong correlation suggests that the rate-limiting step involves chemisorption, characterized by the sharing or exchange of electrons between the Lewis acidic sites and the functional groups of the tetrahydropyridine derivative.[67] This behavior is consistent with the complex nature of multicomponent reaction pathways where intermediate stability on the catalyst surface is crucial.[68] The kinetic data confirm that the formation and stabilization of product (**4a**) on the GO@APTES@DCDA@Sb^{3+} surface follow a pseudo-second order mechanism, establishing chemisorption as the predominant interaction governing the system.

The influence of temperature on the adsorption process was evaluated to determine the thermodynamic feasibility and nature of the reaction. The standard Gibbs free energy ($\Delta G^{\ddagger}$), enthalpy ($\Delta H^{\ddagger}$), and entropy ($\Delta S^{\ddagger}$) were derived from the formula (Table 6):[68,69]

$$\Delta G^{\ddagger} = \Delta H^{\ddagger} - T\Delta S^{\ddagger}$$

$$\Delta G^{\ddagger} = -RT\ln(K_c)$$

$$\ln(K_c) = \frac{\Delta S^{\ddagger}}{R} - \frac{\Delta H^{\ddagger}}{RT}$$

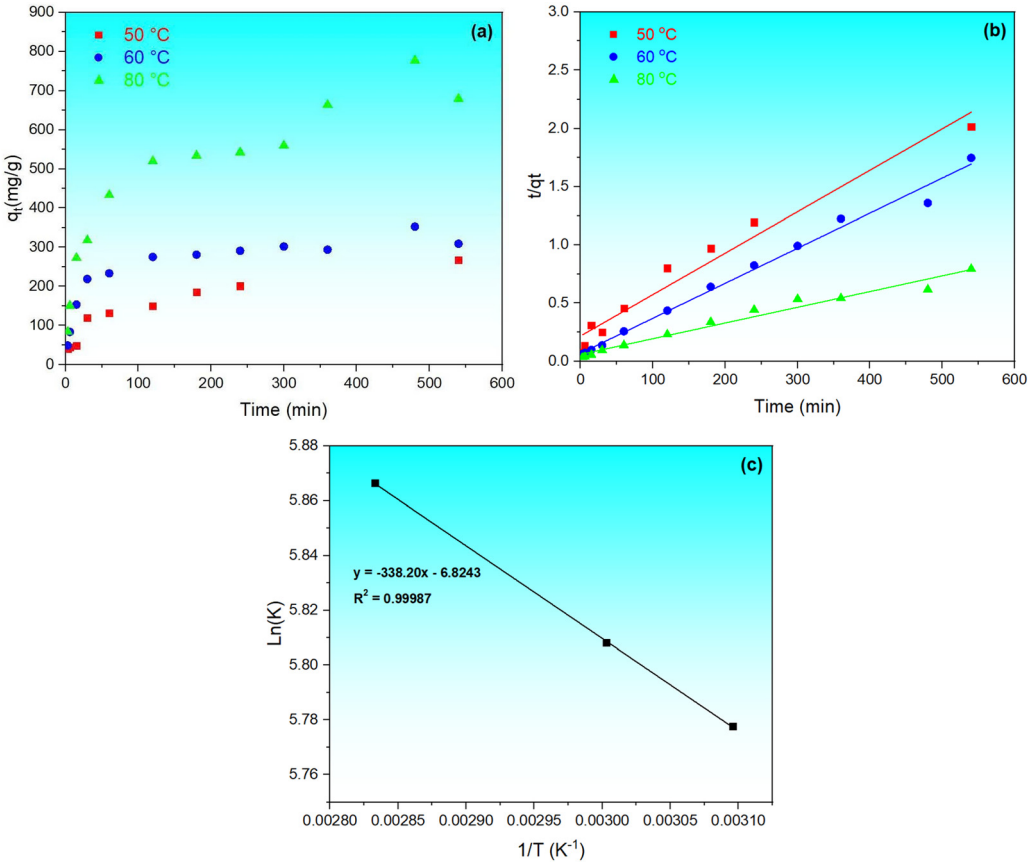

Fig. 9 (a) Adsorbate uptake per unit mass of catalyst as a function of time, (b) pseudo-second order model, and (c) plot of $1/T$ against $\ln K$ for thermodynamic studies.

where K_c is the thermodynamic equilibrium constant, calculated as the ratio of the calculated equilibrium adsorption capacity ($q_{e(cal)}$) to the equilibrium concentration (C_e), and R is the universal gas constant (8.314 J mol^{-1} K^{-1}).

The enthalpy ($\Delta H^{\ddagger}$) was found to be 0.9571 kJ mol^{-1}, which confirms that the adsorption of (**4a**) onto the catalyst surface is an endothermic process. This aligns with the observation that increasing the temperature from 50 to 80 °C led to a significant enhancement in the adsorption capacity. The endothermic nature suggests that thermal energy is required to facilitate the diffusion of reactants and overcome the activation barrier on the solid catalyst.[69] The Gibbs free energy values ($\Delta G^{\ddagger}$) were positive, ranging from 14.23 to 14.66 kJ mol^{-1}, and showed a slight increase with temperature, indicating that the adsorption is a non-spontaneous process under the investigated conditions (Table 6). This non-spontaneity is common in catalytic systems where continuous energy input is necessary to drive the formation of complex cyclic products *via* MCR.[68] Moreover, the negative entropy ($\Delta S^{\ddagger}$) indicates a decrease in the degree of randomness at the solid–liquid interface. This suggests that the product (**4a**) molecules achieve a more ordered and stable orientation upon binding to the active sites of the GO@APTES@DCDA@Sb^{3+} catalyst.[67]

Overall, the combination of a positive $\Delta G^{\ddagger}$, a small positive $\Delta H^{\ddagger}$, and a negative $\Delta S^{\ddagger}$ reveals that while the process is endothermic and non-spontaneous, the increased temperature effectively compensates for the energy requirements, promoting a more organized and stable adsorption of the target compound onto the catalyst.

Table 5 Parameters of pseudo-second order and thermodynamic values

	Temperature (°C)		
Parameters	50	60	80
R^2	0.9658	0.9902	0.9730
a	0.0036	0.0030	0.0014
b	0.2171	0.0686	0.0589
K (g mg^{-1} min^{-1})	0.005	0.006	0.007
$q_{e(cal)}$ (mg g^{-1})	281	332	740
$q_{e(exp)}$ (mg g^{-1})	268	353	777

Table 6 Gibbs free energy ($\Delta G^{\ddagger}$), enthalpy ($\Delta H^{\ddagger}$), and entropy ($\Delta S^{\ddagger}$) values at different conditions

	Temperature (°C)		
Parameters	50	60	80
$\Delta G^{\ddagger}$ (kJ mol^{-1})	14.23	14.37	14.66
$\Delta H^{\ddagger}$ (kJ mol^{-1})	0.9571		
$\Delta S^{\ddagger}$ (kJ mol^{-1} K^{-1})	−0.0144		

2.4. Proposed reaction mechanism for the synthesis of (4a)

Based on previously reported mechanisms, a plausible mechanistic pathway for the formation of piperidines is proposed and depicted in Scheme 5.[70] In the initial step, the β-ketoester and aldehyde undergo condensation with aniline in the presence of GO@APTES@DCDA@Sb^{3+}, affording enaminone and imine intermediates through coordination with the carbonyl functionalities. The enaminone subsequently engages in a Knoevenagel condensation with the aldehyde to generate the reactive intermediate (A). This species, together with the imine formed in the first step, can follow two possible pathways: (i) an aza-Diels–Alder cyclization or (ii) a tandem Mannich–Michael sequence, ultimately leading to the construction of the functionalized piperidine framework (Scheme 5). In the aza-Diels–Alder pathway, the *exo* approach results in the *syn* isomer (**5a**), whereas the *endo* approach affords the *anti* isomer (**4a**). Under the employed reaction conditions, the *anti* isomer was obtained as the predominant product, which can be rationalized by the fact that at elevated temperature (50 °C), the thermodynamically favored product is formed, overriding the stabilization effect provided by the charge-transfer complex.[71]

2.5. Reusability of the GO@APTES@DCDA@Sb^{3+} catalyst in the synthesis of (4a)

The reuse of catalysts is an important aspect of environmentally friendly chemical processes. In this study, the GO@APTES@DCDA@Sb^{3+} catalyst was subjected to a systematic recycling procedure to evaluate its reusability. After each reaction cycle, the catalyst was recovered by filtration, washed thoroughly with acetone, and dried before being applied in subsequent reactions. The variation in catalytic performance across four consecutive cycles is presented in Fig. 10. A gradual decline in activity was observed, which may be attributed to several factors such as structural deterioration, impurity deposition, or reduction in the number of active sites. In addition, catalyst loss during the recovery steps can also contribute to the reduced performance. Nevertheless, even after four cycles, the catalyst was still able to provide a moderate yield of around 30%. The characterization of

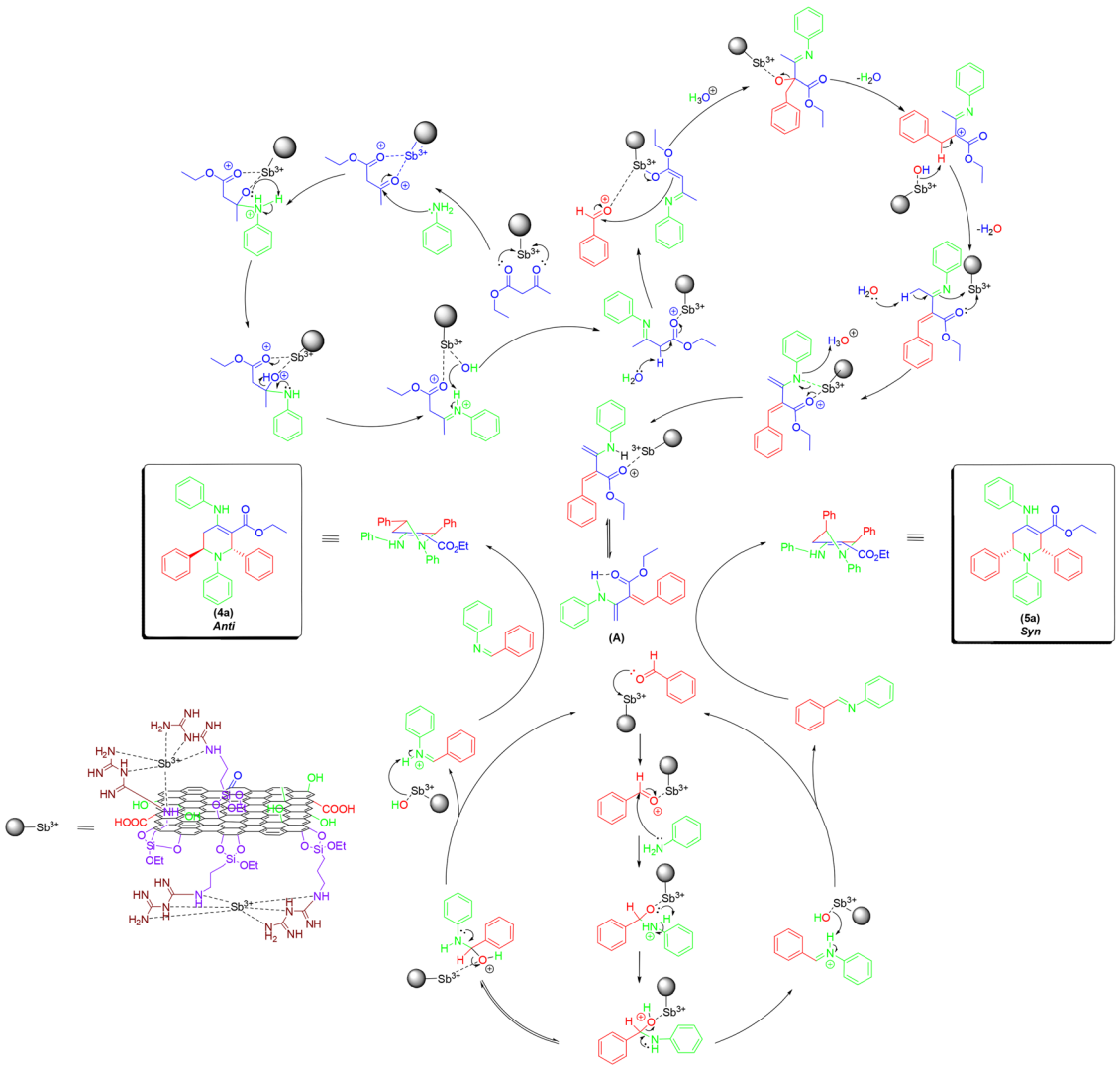

Scheme 5 A proposed reaction mechanism.

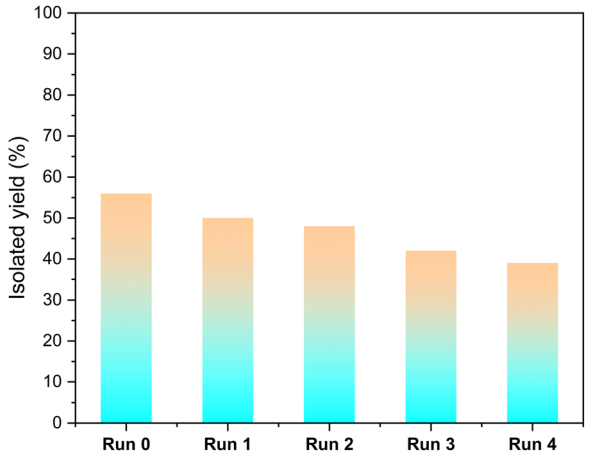

Fig. 10 Reusability of GO@APTES@DCDA@Sb^{3+}.

the GO@APTES@DCDA@Sb^{3+} catalyst before and after recovery revealed notable structural and compositional changes that affected its performance. The FT-IR spectra confirm the presence of characteristic functional groups such as OH, Si–OH, C═O, C═C, N–H, C–O, and Si–O–C, indicating the successful functionalization of GO (Fig. S3). The spectral changes suggest the GO@APTES@DCDA@Sb^{3+} catalyst undergoes structural modifications during use. The loss or transformation of functional groups, coupled with potential contamination, may explain the observed decrease in catalytic activity over successive reaction cycles. The XRD patterns reveal that after the recovery process, the material shows enhanced crystallinity compared to the initial composite (Fig. S4). SEM images demonstrate the layered and porous morphology, with clear structural changes after modification (Fig. S5). The EDX spectrum and elemental analysis further confirm the composition of the material, showing the presence of C, O, Si, and Sb, consistent with the designed structure (Fig. S6 and S7). However, after 4 times of recovery and reuse of GO@APTES@DCDA@Sb^{3+}, the atom% of Sb decreased from 1.85% to 1.38%, which can be considered as the reason for the decrease in the yield of product (**4a**) from 56% to about 40%. The remaining Sb element content in the GO@APTES@DCDA@Sb^{3+} catalyst after four times of recovery and reuse, recorded by ICP-MS method as 7.42 mmol g^{-1}.

2.6. Large-scale synthesis of (4a)

Following Scheme 6, the optimal conditions were applied to scale up the multi-component reaction for the synthesis of (**4a**) from benzaldehyde (50 mmol), aniline (50 mmol), ethyl acetoacetate (25 mmol) in the presence of GO@APTES@DCDA@Sb^{3+} (100 mg). The reaction was carried out at 50 °C for 380 minutes under solvent-free conditions, affording a good yield of 57% with no significant loss in conversion. The *syn–anti* (**5a : 4a**) ratio of the products was recorded as diastereomeric ratio of 9 : 91.

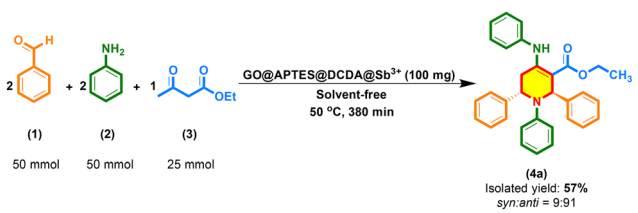

Scheme 6 Investigation of scale-up in the (**4a**) production process utilizing the GO@APTES@DCDA@Sb^{3+} catalyst.

2.7. Control reaction

From Table S2, the multicomponent reaction among ethyl acetoacetate, benzaldehyde, and aniline in optimized conditions resulted in a modest yield of approximately 56%. To examine the cause of this relatively low efficacy, a series of control experiments were devised and conducted in which different combinations of substrates were subject to the same optimized conditions. The results revealed important trends. First, the use of aniline and benzaldehyde individually (entries 1 and 2, Table S2) was unproductive, showing that condensation does not take place under present conditions. Whenever aniline and benzaldehyde were combined in different molar ratios (entries 3–6, 8–9, 13, 16, 21, 24, 26, and 28, Table S2), the reaction always yielded the same kind of product, pointing to a selective transformation precluding the multicomponent adduct we were looking for.[72,73] On the other hand, the reaction of aniline with ethyl acetoacetate gave rise to isolated products in a number of instances (entries 7, 10, 14, 23, and 25, Table S2), attesting to the intrinsic reactivity of this substrate combination.[74] Conversely, the combination of benzaldehyde and ethyl acetoacetate was unfruitful, eliminating the binary pathway as a side reaction. Notably, whenever the three substrates-benzaldehyde, aniline, and ethyl acetoacetate-were combined in different molar ratios, the reaction gave a complex product. In addition to the target compound, a number of side products formed, including those of control reactions and others unique to the ternary system (entries 15, 18, and 23, Table S2).[75] The fact that two parallel pathways operate demonstrates that the low yield of the target compound is the result of the competitive formation of undesired side products. These control experiments underscore the competitiveness of the reaction system. While multicomponent transformation is possible, its efficiency is compromised by side reactions among binary substrates. This result explains the modest yield and indicates that further optimization or more selective catalysts may reduce side-products.

2.8. Leaching test experiment

A leaching test was conducted to assess the stability of the GO@APTES@DCDA@Sb^{3+} catalyst and to quantify the potential leaching of the active antimony, Sb^{3+}, into the reaction media. In this experiment, a mixture of aniline (6 mmol), ethyl acetoacetate (3 mmol), and the GO@APTES@DCDA@Sb^{3+} catalyst (12 mg) was stirred at room temperature for 20 minutes. Subsequently, benzaldehyde (6 mmol) was introduced, and the reaction mixture was stirred at 50 °C. After 3 h of reaction time, the mixture was divided into three parts (Fig. 11). The concentration of Sb^{3+} in the solution was monitored using ICP-MS to evaluate the catalyst's heterogeneity and stability.

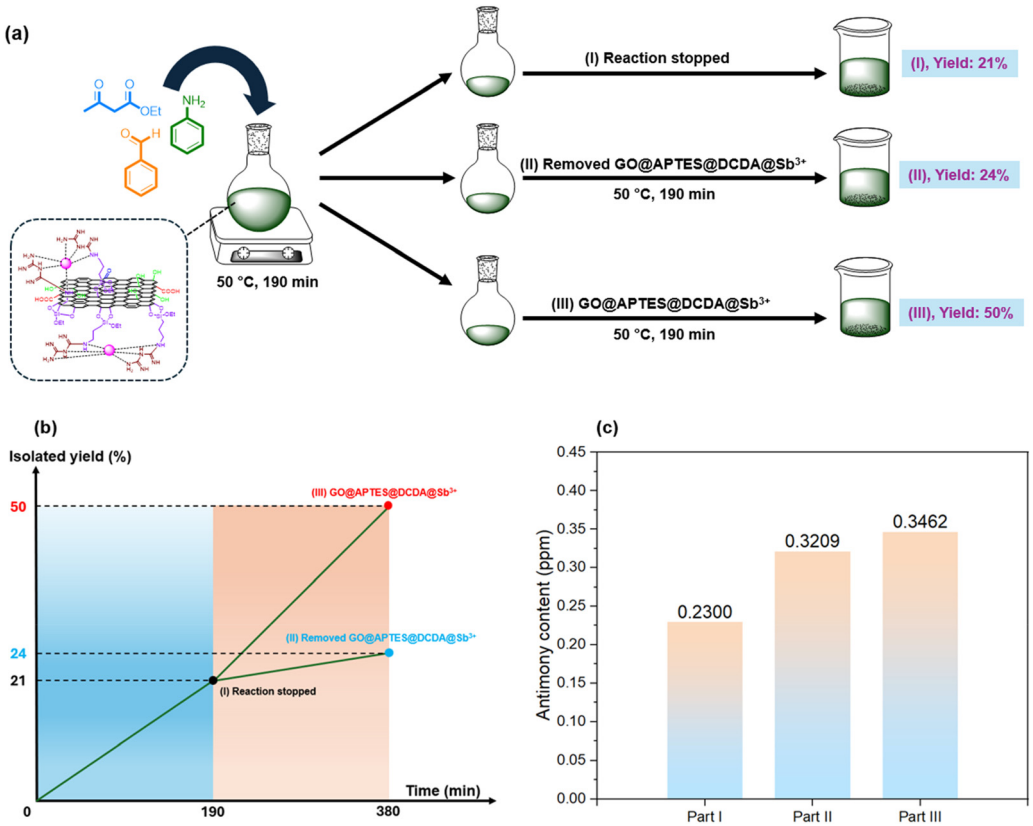

Fig. 11 (a) Leaching test procedure, (b) leaching test production yield over time, and (c) ICP-MS analysis of Sb^{3+}. Part I: stop reaction; part II: continue the reaction without GO@APTES@DCDA@Sb^{3+}; and part III: continue the reaction with GO@APTES@DCDA@Sb^{3+}.

In part I, the catalyst was removed from the reaction mixture *via* filtration. The resulting solution was then subjected to crystallization in 5 mL of ethanol, which afforded the final product with a yield of approximately 21%. This initial step confirms that the reaction has commenced, although it is far from complete. ICP-MS analysis of the filtrate indicated that the concentration of leached Sb^{3+} was 0.23 ppm, suggesting minimal loss of the active metal from the support during the first half of the reaction.

In part II, the catalyst was also filtered out, and the remaining solution was allowed to continue reacting for an additional 3 h. Upon work-up and crystallization, the product was obtained in approximately 24% yield, with a measured Sb^{3+} concentration of 0.32 ppm. The insignificant increase in the reaction's yield after catalyst separation indicates the essential role of the catalyst, which the reaction did not proceed remarkably in its absence.

In part III, the reaction mixture was allowed to continue for an additional 3 h without the GO@APTES@DCDA@Sb^{3+} catalyst. After the full reaction time, the catalyst was separated, and the product was crystallized in 5 mL of ethanol, achieving a final yield of approximately 50%. The concentration of leached Sb^{3+} was determined to be 0.35 ppm. In comparison with part II, it demonstrates that the catalyst is required throughout the reaction to achieve a high yield; furthermore, the leaching of the active Sb^{3+} is negligible, highlighting the catalyst's excellent stability and efficiency.

2.9. Assessment of green metrics

Over the past few years, the push for eco-conscious and sustainable methodologies in organic synthesis has intensified. At the heart of this movement is green chemistry, which seeks to minimize toxic waste and maximize resource efficiency. A notable advancement in this field is the use of the GO@APTES@DCDA@Sb^{3+} catalyst for constructing 1,2,5,6-tetrahydropyridine-3-carboxylate frameworks. The sustainability of this approach is evidenced by an *E*-factor of 0.11, representing a drastic reduction in waste compared to traditional methods.[76] Furthermore, the atom economy (AE) reached 89.78%, though the actual atom efficiency (AEf) was lower at 50.28%, indicating that while most reactant atoms are theoretically accounted for, some loss still occurs during the actual process. With a process mass intensity (PMI) of 1.99, this technique is significantly more material-efficient than conventional syntheses, which often exceed a PMI of 10.[77] While the carbon efficiency (CE) of 56.0% and reaction mass efficiency (RME) of 50.24% suggest room for improvement in carbon integration and yield-to-mass correlation, they still outperform older methods that typically see RMEs as low as 20%.[78] Overall, an eco-score of 68.0% highlights the environmental benefits of

this catalytic system, though further refinements in atom and carbon utilization are needed to fully realize green chemistry ideals.[79–82] (The computed data is provided in the SI.)

2.10. Comparison of this work to previous work

To demonstrate this work's merit relative to the literature (Table 7), we compared the performance of GO@APTES@DCDA@Sb^{3+} with four reported catalysts (BDMS, TBATB, $InCl_3$, and VCl_3) for the synthesis of 1,2,5,6-tetrahydropyridine-3-carboxylate.[83–86] Reusability has become a key attribute for practical catalysts; unlike the literature catalysts, which were reported to be difficult to separate from the reaction media, our catalyst was readily separated and recovered. Furthermore, our solvent-free protocol reached completion in 380 min (6 h 20 min), achieving comparable yields while offering clear operational advantages in catalyst recovery and process simplicity.

3. Experimental section

3.1. Preparation of GO@APTES@DCDA@M^{n+} from *Manihot esculenta* branches, leaves

3.1.1. Preparation of GO (graphene oxide). The roots of *Manihot esculenta* were initially removed, as they constitute the edible portions. The remaining branches and leaves were ground and subsequently carbonized in an inert atmosphere at 600 °C for 3 h. GO was synthesized from the resulting graphite using the modified Hummers' method.[40]

3.1.2. Preparation of GO@APTES. APTES was functionalized onto GO following the method described in a previously reported publication.[42] GO (0.1 g), triethylamine (1.8 mL), APTES (1.0 mL), toluene (10 mL) were added to a 25 mL round-bottom flask and stirred at 800 rpm for 10 min. The mixture was refluxed at 120 °C for 6 h to obtain a light brownish-black material. Subsequently, the reaction was allowed to cool to room temperature before being diluted with 5–10 mL of diethyl ether and transferred to a 100 mL beaker. The stir bar was separated using an external magnet and washed with diethyl ether, simultaneously; then it was removed from the reaction mixture. The remaining solution was washed and decanted with diethyl ether (5 × 10 mL). Finally, the final product was dried at room temperature under ambient conditions.

3.1.3. Preparation of GO@APTES@DCDA. GO@APTES (0.1 g), triethylamine (1.8 mL), dicyandiamide (25 mg) were mixed in a 25 mL round-bottom flask and stirred at 800 rpm for 10 min before being heated at 65 °C for 24 h. The resulting black solid was then transferred into a 100 mL beaker with 5–10 mL of diethyl ether; the stir bar was separated, washed, and removed from the reaction media as previously described. GO@APTES@DCDA was obtained after drying at room temperature under ambient conditions.[43]

3.1.4. Preparation of GO@APTES@DCDA@M^{n+}. GO@APTES@DCDA (0.1 g), metal halide (0.2 g), and ethanol (3 mL) were added to a 25 mL round-bottom flask and sonicated for 10 min before being assembled into a reflux system. The mixture was then refluxed under a nitrogen atmosphere at 80 °C for 8 h. After completion, the resulting solid was obtained by rotary evaporation at 60 °C under reduced pressure.[44]

3.2. General procedure for the synthesis of 1,2,5,6-tetrahydropyridine-3-carboxylate derivatives

In 25 mL round-bottom flask, a mixture of aniline (1 mmol), ethyl acetoacetate (0.5 mmol), and the GO@APTES@DCDA@Sb^{3+} was stirred at 500 rpm for 20 min at room temperature. Then, benzaldehyde (1 mmol) was added, and the mixture was stirred at 50 °C for 6 h. The reaction progress was monitored by thin-layer chromatography (TLC). Once completion, the catalyst was separated and washed with acetone (5 × 3 mL). Crystallization was induced by adding 5 mL of ethanol to the filtration. After crystal formation, the product was washed with cold ethanol and recrystallized from ethanol (5 mL). The product was washed with cold ethanol (5 × 3 mL). The purity and structure of the product were confirmed by melting point, HRMS(ESI), ^{1}H-NMR, and ^{13}C-NMR spectroscopy.

4. Conclusion

In this work, a novel multifunctional catalyst, GO@APTES@DCDA@Sb^{3+}, was successfully synthesized from *Manihot esculenta* biomass through sequential surface functionalization and metal coordination. Detailed characterization confirmed the incorporation of nitrogen-rich groups and uniformly dispersed Sb^{3+} ions, providing abundant Lewis acidic sites. Comprehensive characterization of the catalyst was carried out through FT-IR, EDX, EDX-mapping, XRD, Raman, SEM, and XPS. The catalyst exhibited good activity in the solvent-free multicomponent condensation synthesis of 1,2,5,6-tetrahydropyridine-3-carboxylate derivatives (isolated yield up to 56%), affording high diastereoselectivity and satisfactory yields under mild conditions. The *anti*-isomer was obtained with diastereomeric ratios (dr) up to 90 : 10–100 : 0. Kinetic assessments were conducted to confirm the catalyst's effectiveness in the newly developed reaction. Derived thermodynamic parameters showed $\Delta H^{\ddagger} = 0.9571$ kJ mol^{-1} and $\Delta S^{\ddagger} = -0.0144$ kJ mol^{-1} K^{-1}; notably, $\Delta G^{\ddagger}$ was found to increase progressively as a function of temperature. Importantly, GO@APTES@DCDA@Sb^{3+} demonstrated good recyclability

Table 7 Comparative study with a reported method for the synthesis of fused 1,2,5,6-tetrahydropyridine-3-carboxylate

Entry	Reaction conditions	Temp. (°C)	Time (h)	Yield (%)	Ref.
1	Bromodimethylsulfonium bromide (BDMS) (10 mol%), acetonitrile (5 mL)	rt.	6	38	84
2	Tetrabutylammonium tribromide (TBATB) (0.1 mmol), EtOH (5 mL)	rt.	24	74	85
3	$InCl_3$ (0.67 mmol), acetonitrile (4 mL)	rt.	24	60	83
4	VCl_3 (0.1 mmol), EtOH (5 mL)	rt.	7.5	73	86
5	GO@APTES@DCDA@Sb^{3+} (5 mg), solvent-free	50	6.2	56	This work

and structural stability with negligible metal leaching, retaining catalytic performance. The method is environmentally friendly since the solid catalyst can be recovered and reused for several cycles.

Author contributions

Tuan Minh Dang: investigation, methodology, resources, formal analysis, validation, data curation, and writing – original draft; The-Anh Trinh Duong: investigation, formal analysis, validation, data curation, and writing – original draft; Trung-Nhan Dong Tran: resources, formal analysis, validation, and data curation; Hai Truong Nguyen: methodology, resources, formal analysis, validation, data curation, writing – review and editing, and supervision.

Conflicts of interest

The authors declare that they have no known competing financial interests or personal relationships that could have appeared to influence the work reported in this paper.

Data availability

The data supporting this article have been included as part of the main text and supplementary information (SI). Supplementary information available. See DOI: https://doi.org/10.1039/d5ma01346a.

Acknowledgements

This research is funded by Vietnam National University, Ho Chi Minh City (VNU-HCM) under grant number B2025-18-05.

References

1 R. P. Lee, *J. Cleaner Prod.*, 2019, **219**, 786–796.
2 A. Arevalo-Gallegos, Z. Ahmad, M. Asgher, R. Parra-Saldivar and H. M. N. Iqbal, *Int. J. Biol. Macromol.*, 2017, **99**, 308–318.
3 L. M. de Souza Mesquita, L. S. Contieri, F. A. e Silva, R. H. Bagini, F. S. Bragagnolo, M. M. Strieder, F. H. B. Sosa, N. Schaeffer, M. G. Freire, S. P. M. Ventura, J. A. P. Coutinho and M. A. Rostagno, *Green Chem.*, 2024, **26**, 10087–10106.
4 W.-J. Liu, H. Jiang and H.-Q. Yu, *Chem. Rev.*, 2015, **115**, 12251–12285.
5 D. Laishram, S.-B. Kim, S.-Y. Lee and S.-J. Park, *Adv. Sci.*, 2025, **12**, 2410383.
6 H. He, R. Zhang, P. Zhang, P. Wang, N. Chen, B. Qian, L. Zhang, J. Yu and B. Dai, *Adv. Sci.*, 2023, **10**, 2205557.
7 A. D. A. Bin Abu Sofian, X. Sun, V. K. Gupta, A. Berenjian, A. Xia, Z. Ma and P. L. Show, *Energy Fuels*, 2024, **38**, 1593–1617.
8 V. Georgakilas, J. N. Tiwari, K. C. Kemp, J. A. Perman, A. B. Bourlinos, K. S. Kim and R. Zboril, *Chem. Rev.*, 2016, **116**, 5464–5519.
9 H. Shang, Y. Zhang, Y. Dong, Y. Zhu and C. Pan, *ChemCatChem*, 2025, **17**, e202402062.
10 C. Hu, Y. Yang, Y. Lin, L. Wang, R. Ma, Y. Zhang, X. Feng, J. Wu, L. Chen and L. Shao, *Adv. Drug Delivery Rev.*, 2021, **178**, 113967.
11 J. Guerrero-Contreras and F. Caballero-Briones, *Mater. Chem. Phys.*, 2015, **153**, 209–220.
12 A. F. Betancur, N. Ornelas-Soto, A. M. Garay-Tapia, F. R. Pérez, Á. Salazar and A. G. García, *Mater. Chem. Phys.*, 2018, **218**, 51–61.
13 X. Huang, Z. Yin, S. Wu, X. Qi, Q. He, Q. Zhang, Q. Yan, F. Boey and H. Zhang, *Small*, 2011, **7**, 1876–1902.
14 C. Chen, S. Zhang, B. Huang, Y. Peng, Y. Zhang, L. Wang and Y. Wang, *Adv. Funct. Mater.*, 2024, **34**, 2410248.
15 T.-P. H. Dang, T. N. Pham, P. H. Tran and H. T. Nguyen, *Mater. Adv.*, 2025, **6**, 3314–3330.
16 S. Mondal, B. C. Patra and A. Bhaumik, *ChemCatChem*, 2017, **9**, 1469–1475.
17 C. Rizescu, M. El Fergani, D.-I. Eftemie, B. Cojocaru, D. Popescu, M. Andruh and V. I. Parvulescu, *Appl. Catal., A*, 2023, **663**, 119302.
18 C. Su and K. P. Loh, *Acc. Chem. Res.*, 2013, **46**, 2275–2285.
19 S. Suleman, H. A. Younus, Z. A. K. Khattak, H. Ullah, M. Elkadi and F. Verpoort, *J. Mol. Catal.*, 2020, **493**, 111071.
20 F. Dadvar and D. Elhamifar, *Nanoscale Adv.*, 2024, **6**, 5398–5408.
21 V. V. Gaikwad, V. B. Saptal, K. Harada, T. Sasaki, D. Nishio-Hamane and B. M. Bhanage, *ChemNanoMat*, 2018, **4**, 575–582.
22 E. B. Dennler and A. R. Frasca, *Can. J. Chem.*, 1967, **45**, 697–705.
23 N. König, Y. Godínez-Loyola, F. Yang, C. Laube, M. Laue, P. Lönnecke, C. A. Strassert and E. Hey-Hawkins, *Chem. Sci.*, 2023, **14**, 2267–2274.
24 H. B. Phan, C. M. Luong, L. P. Nguyen, B. T. Bui, H. T. Nguyen, B. V. Mai, T. V. T. Mai, L. K. Huynh and P. H. Tran, *ACS Sustainable Chem. Eng.*, 2022, **10**, 8673–8684.
25 A. Rathore, V. Asati, S. K. Kashaw, S. Agarwal, D. Parwani, S. Bhattacharya and C. Mallick, *Mini-Rev. Med. Chem.*, 2021, **21**, 362–379.
26 C. Yang, S. Zhang and J. Hou, *Aggregate*, 2022, **3**, e111.
27 M. M. Abdelshaheed, I. M. Fawzy, H. I. El-Subbagh and K. M. Youssef, *Future J. Pharm. Sci.*, 2021, **7**, 188.
28 R. Mohan Malothu and G. Thalari, *Chem. Biodiversity*, 2025, **22**, e202402223.
29 G. Pavale, P. Acharya, N. Korgavkar and M. M. V. Ramana, *Curr. Comput.-Aided Drug Des.*, 2022, **18**, 414–424.
30 P. C. B. Halicki, I. L. Pereira, N. Zanatta, V. P. de Andrade, P. E. Almeida da Silva and D. F. Ramos, *Tuberculosis*, 2022, **136**, 102252.
31 J. S. Vianna, I. B. Ramis, D. Bierhals, A. von Groll, D. F. Ramos, N. Zanatta, M. C. Lourenço, M. Viveiros and P. E. Almeida da Silva, *J. Global Antimicrob. Resist.*, 2019, **17**, 296–299.
32 V. K. Sharma and S. K. Singh, *RSC Adv.*, 2017, **7**, 2682–2732.
33 M. Gamper, H. Gstach and J. G. Schantl, *Monatsh. Chem.*, 2023, **154**, 1419–1425.

34 S. K. Bora and A. K. Saikia, *RSC Adv.*, 2025, **15**, 21257–21268.
35 A. C. Shaikh and O. Kwon, *Org. Synth.*, 2019, **96**, 110–123.
36 P. M. Davanagere, M. De, K. Chanda and B. Maiti, *Catalysts*, 2023, **13**, 209.
37 I. Coldham, A. J. Collis, R. J. Mould and R. E. Rathmell, *J. Chem. Soc., Perkin Trans. 1*, 1995, 2739–2745.
38 M. G. Vinogradov, O. V. Turova and S. G. Zlotin, *Adv. Synth. Catal.*, 2021, **363**, 1466–1526.
39 F.-X. Felpin and J. Lebreton, *Tetrahedron Lett.*, 2003, **44**, 527–530.
40 G. Supriyanto, N. K. Rukma, A. K. Nisa, M. Jannatin, B. Piere, A. Abdullah, M. Z. Fahmi and H. S. Kusuma, *BioResources*, 2018, **13**, 4832–4840.
41 J. P. Rodríguez-Caicedo, D. R. Joya-Cárdenas, A. Gallegos-Muñoz, M. R. Abraham-Juárez, M. Zapata-Torres, C. E. Damián-Ascencio and A. Saldaña-Robles, *Results Eng.*, 2025, **25**, 104189.
42 Subodh, N. K. Mogha, K. Chaudhary, G. Kumar and D. T. Masram, *ACS Omega*, 2018, **3**, 16377–16385.
43 A. Mishra, P. Yadav and S. K. Awasthi, *ACS Org. Inorg. Au*, 2023, **3**, 254–265.
44 M. Sypabekova, A. Hagemann, D. Rho and S. Kim, *Biosensors*, 2023, **13**, 36.
45 Y. Ban, Q. Liu, H. Zhou, R. He, K. Zhi and N. Li, *Energy Fuels*, 2019, **33**, 12182–12190.
46 H. T. Nguyen, T. V. Le and P. H. Tran, *J. Environ. Chem. Eng.*, 2021, **9**, 105228.
47 V. Brusko, A. Khannanov, A. Rakhmatullin and A. M. Dimiev, *Carbon*, 2024, **229**, 119507.
48 A. R. Deline, B. P. Frank, C. L. Smith, L. R. Sigmon, A. N. Wallace, M. J. Gallagher, D. G. Goodwin, Jr., D. P. Durkin and D. H. Fairbrother, *Chem. Rev.*, 2020, **120**, 11651–11697.
49 I. F. Sáez del Bosque, S. Martínez-Ramírez and M. T. Blanco-Varela, *Constr. Build. Mater.*, 2014, **52**, 314–323.
50 J. Ren, F. Weber, F. Weigert, Y. Wang, S. Choudhury, J. Xiao, I. Lauermann, U. Resch-Genger, A. Bande and T. Petit, *Nanoscale*, 2019, **11**, 2056–2064.
51 Y. Qin, J. Lu, X. Zhao, X. Lin, Y. Hao, P. Huo, M. Meng and Y. Yan, *J. Chem. Eng.*, 2021, **425**, 131844.
52 M. Shang, S. Liang, N. Qu, H. Lian and J. Lin, *Chem. Mater.*, 2017, **29**, 1813–1829.
53 G. Yuan, X. Li, Z. Dong, A. Westwood, Z. Cui, Y. Cong, H. Du and F. Kang, *Carbon*, 2012, **50**, 175–182.
54 A. A. L. Sales, C. M. B. D. E. M. Barbosa, A. G. Câmara, E. E. Silva, L. G. T. C. Melo, J. G. A. Pacheco, J. A. P. da Costa, R. Santos-Oliveira, M. V. F. Lima, R. M. Santos and F. D. Menezes, *Carbon*, 2025, **234**, 119988.
55 Y. Li, Y.-H. Zhao, L.-L. Zhao, P.-F. Wang, Y. Xie and T.-F. Yi, *Rare Met.*, 2024, **43**, 2994–3006.
56 A. Kathalingam, D. Vikraman, K. Karuppasamy and H.-S. Kim, *Ceram. Int.*, 2022, **48**, 28906–28917.
57 C. Cheng, Q. Guo, L. Ding, Y. Gong and G. Yu, *J. Cleaner Prod.*, 2024, **448**, 141701.
58 G. Chakraborty, R. Padmashree and A. Prasad, *Mater. Sci. Eng. B*, 2023, **297**, 116817.
59 Y. Wan, C. Fang, X. Yang, J. Liu and Y. Lin, *J. Mater. Chem. A*, 2024, **12**, 33392–33426.
60 S. Movaghgharnezhad and P. Kang, *J. Mater. Chem. C*, 2024, **12**, 6718–6742.
61 J. Senthilnathan, Y.-F. Liu, K. S. Rao and M. Yoshimura, *Sci. Rep.*, 2014, **4**, 4395.
62 M. C. Biesinger, *Appl. Surf. Sci.*, 2022, **597**, 153681.
63 I.-Y. Jeon, M. Choi, H.-J. Choi, S.-M. Jung, M.-J. Kim, J.-M. Seo, S.-Y. Bae, S. Yoo, G. Kim, H. Y. Jeong, N. Park and J.-B. Baek, *Nat. Commun.*, 2015, **6**, 7123.
64 R. S. Alruwais, W. A. Adeosun, H. M. Marwani, M. Jawaid, A. M. Asiri and A. Khan, *Polymers*, 2021, **13**, 2562.
65 H. Li, H. Jin, R. Li, J. Hua, Z. Zhang and R. Li, *Sci. Rep.*, 2024, **14**, 1217.
66 E. Alptekin and M. Canakci, *Fuel*, 2010, **89**, 4035–4039.
67 G. H. C. Oliveira, L. M. Ramos, R. K. C. de Paiva, S. T. A. Passos, M. M. Simões, F. Machado, J. R. Correa and B. A. D. Neto, *Org. Biomol. Chem.*, 2021, **19**, 1514–1531.
68 A. Dueñas-Deyá, R. E. Cordero-Rivera and M. Martínez-Vázquez, *ACS Omega*, 2026, **11**, 2687–2702.
69 N. Sharma, B. Chowhan, M. Gupta and M. Kouser, *Dalton Trans.*, 2022, **51**, 13795–13807.
70 B. Umamahesh, V. Sathesh, G. Ramachandran, M. Sathishkumar and K. Sathiyanarayanan, *Catal. Lett.*, 2012, **142**, 895–900.
71 C. Mukhopadhyay, S. Rana, R. J. Butcher and A. M. Schmiedekamp, *Tetrahedron Lett.*, 2011, **52**, 5835–5840.
72 C.-C. Wang, Y. Tang, Y.-H. Pan, J. Yang and Y.-M. Zhang, *Tetrahedron Lett.*, 2015, **56**, 2863–2866.
73 A. Subashini, V. Veeramani, K. Thamaraiselvi, A. Crochet, P. Rose, R. Philip, R. R. Babu and K. Ramamurthi, *Opt. Mater.*, 2021, **117**, 111081.
74 S. R. Mousavi, H. Sereshti, H. Rashidi Nodeh and A. Foroumadi, *Appl. Organomet. Chem.*, 2019, **33**, e4644.
75 A. T. Khan, M. M. Khan and K. K. R. Bannuru, *Tetrahedron*, 2010, **66**, 7762–7772.
76 R. A. Sheldon, *Green Chem.*, 2023, **25**, 1704–1728.
77 E. R. Monteith, P. Mampuys, L. Summerton, J. H. Clark, B. U. W. Maes and C. R. McElroy, *Green Chem.*, 2020, **22**, 123–135.
78 A. P. Dicks and A. Hent, in *Green Chemistry Metrics: A Guide to Determining and Evaluating Process Greenness*, ed. A. P. Dicks and A. Hent, Springer International Publishing, Cham, 2015, pp. 17–44, DOI: 10.1007/978-3-319-10500-0_2.
79 R. A. Sheldon, *ACS Sustainable Chem. Eng.*, 2018, **6**, 32–48.
80 D. J. C. Constable, A. D. Curzons and V. L. Cunningham, *Green Chem.*, 2002, **4**, 521–527.
81 K. Van Aken, L. Strekowski and L. Patiny, *Beilstein J. Org. Chem.*, 2006, **2**, 3.
82 N. Sahiba, A. Sethiya, J. Soni and S. Agarwal, *ChemistrySelect*, 2020, **5**, 13076–13080.
83 P. A. Clarke, A. V. Zaytzev and A. C. Whitwood, *Tetrahedron Lett.*, 2007, **48**, 5209–5212.
84 A. T. Khan, T. Parvin and L. H. Choudhury, *J. Org. Chem.*, 2008, **73**, 8398–8402.
85 A. T. Khan, M. Lal and M. M. Khan, *Tetrahedron Lett.*, 2010, **51**, 4419–4424.
86 S. Pal, L. H. Choudhury and T. Parvin, *Mol. Diversity*, 2012, **16**, 129–143.